

Contents lists available at ScienceDirect

# Computational Materials Science

journal homepage: [www.elsevier.com/locate/commsci](http://www.elsevier.com/locate/commsci)

## Molecular dynamics simulation of plastic deformation and interfacial delamination of NiTi/Ag bilayer by cyclic-nanoindentation: Effects of crystallographic orientation of substrate

Sara Fazeli\*, Sayed Khatiboleslam Sadrnezhaad

Department of Material Science and Engineering, Sharif University of Technology, PO Box 11155-9466, Tehran, Iran

## ARTICLE INFO

## Keywords:

Cyclic nanoindentation  
 Interfacial delamination  
 Deformation mechanisms  
 Interfacial toughness  
 Jarzynski's equality  
 NiTi/Ag bilayer

## ABSTRACT

This paper presents a comparative study of plasticity and fracture behavior of the NiTi/Ag bilayer for the different crystallographic orientations of the substrate. Molecular dynamic (MD) simulation was used to determine the deformation mechanism, dislocation density, plastic energy dissipation and delamination of the NiTi/Ag bilayers near the interface, when NiTi aligned at (1 0 0), (1 1 1), (1 1 0), (3 2 1), (2 1 0) and (2 1 1) faces during the cyclic-nanoindentation test. The Griffith energy balance model was used to estimate the energy release associated with the delamination. The results of the simulation are suggested the dependence of deformation mechanism, energy release rate ( $G_{in}$ ), interfacial toughness ( $K_{in}$ ) and average plastic energy dissipation per unit cycle ( $E_{plastic}$ ) of NiTi/Ag bilayer on the crystallographic orientation of the NiTi substrate. Prismatic dislocation loop and the nest-like organization of the twins were responsible for the plastic deformation of the NiTi/Ag bilayers when NiTi aligned at (211,010,111) and (100,210,321) faces, respectively. The values of  $G_{in}$  and  $K_{in}$  of the bilayers were in the range of 64.27–147.71 J/m<sup>2</sup> and 77–192 J/m<sup>2</sup>, respectively. The values of  $E_{plastic}$  is increased in the following order: NiTi (2 1 1) < NiTi (3 2 1) < NiTi (1 0 0) < NiTi (2 1 0) < NiTi (1 1 1) < NiTi (0 1 0). The average dislocation densities produced for the indenter radius of 30 Å were in the range of  $1.23 \times 10^{19}$ – $1.84 \times 10^{19} \text{ m}^{-2}$ . The results show that the NiTi (0 1 0)/Ag case has the larger dislocation density than other bilayers. Both of hardness and the interfacial toughness of the NiTi/Ag at different crystallographic orientations were consistent with the free energy data obtained from Jarzynski's equality for nanoindentation results, which were in the range of  $3.35 \times 10^{-4}$ – $7.81 \times 10^{-4} \text{ eV/atom}$ . Due to high interfacial toughness and hardness plus lower plastic energy dissipation, the NiTi (2 1 1)/Ag bilayer may show the better results for engineering and medical applications.

### 1. Introduction

NiTi is a novel material for use in biomedical and microelectromechanical systems (MEMS). The most critical applications are bone-joints, orthodontic components, orthopedic implants, and cardiovascular and urological stents [1–5]. Limited hardness and wear-resistance are barrier to the NiTi versatile usages in such broad areas as dental and MEMS applications [6]. For medical usage, it is vital to optimize the passivation processing of NiTi alloy to prevent the surface layer from degradation [7]. Hence, surface modification with the goal of refinement of the NiTi biocompatibility, abrasion resistance and cell-adherence could be exciting. Deposition of thin coatings made of biocompatible elements or composites can effectively improve the physicochemical and topo-mechanical characteristics of the NiTi

microsurgical tools [8,9]. It is generally agreed that silver with the antibacterial/antitumor capability is a promising candidate for enhancement of the surface properties of the biomedical NiTi alloys [8,10]. Brittleness usually restricts the successful efficiency and reliability of the coatings [11,12]. There is an increasing demand for developing authentic techniques to characterize the deformation and delamination mechanisms of a thin-film and a nano-multilayer. This increase is due to the discovering and understanding of the mechanical behavior and deformation mechanisms, which affect the design, construction, and utilization of the NiTi-based multilayer structures and devices. Among the easily reached techniques, the MD simulation enables the investigation of the defects at atomic-level under nanoindentation, nano-scratching and tension to obtain a detailed understanding of the properties of the film/substrate systems [2,13,14].

\* Corresponding author.

E-mail address: [s.fazeli@sharif.edu](mailto:s.fazeli@sharif.edu) (S. Fazeli).

<https://doi.org/10.1016/j.commsci.2019.05.032>

Received 10 February 2019; Received in revised form 13 May 2019; Accepted 14 May 2019

Available online 07 June 2019

0927-0256 / © 2019 Elsevier B.V. All rights reserved.

The evaluation of the adhesion properties of a thin film is vital to certify the validity of the film/substrate system over its life cycles [15].

During the last decades, there have been a few studies to expand attitudes for the interfacial failure mechanisms and, consequently, the quantification of interfacial strength [16–19]. Numerous challenges related to nanoindentation simulation and experimental works contain the modeling of interface behavior, brittle coating failure and possible interaction between them [20]. Adhesion failure frequently reflects a cracking incident characterizable through an interfacial toughness parameter which, together with the mechanical properties of the coating and substrate, can be applied to estimate the beginning and rate of propagation of failure [21].

Nanoindentation is a useful way to find out about the investigation of interfacial adhesion of a film/substrate system to be undertaken in a controllable procedure through creating interfacial cracks on an adequately small scale and at a particular site [22–24]. The delamination mechanisms of the multilayers underneath nanoindentation are little understood and estimation of the interfacial adhesion still needs in-depth research [25–27]. To the best of our knowledge, the indentation-induced fracture is not well-understood in the case of the NiTi/Ag bilayer. Some models have been used to determine the interfacial toughness ( $K_{in}$ ) or energy release rate ( $G_{in}$ ) through nanoindentation, amid which stress field analysis and energy method being the two central attitudes [28].

Compared to stress analysis, the energy method is known to be more straightforward and practical for nanoindentation testing [23]. For instance, Lu et al. [15] have measured the interfacial adhesion of SiN/GaAs film/substrate systems via a cyclic-nanoindentation based on the energy method. They reported that the cyclic loading nanoindentation was useful for delamination in quite “tough” SiN/GaAs interfaces. Chiang et al. [29] have examined the interfacial strength for the surface coating using the nanoindentation test by a Vickers indenter. They also found that the nanoindentation deformation compacts the coating, leading to the delamination of the coating from the substrate. Coating cracking failure happens when the mechanical work of the brittle failure in the coating is equivalent to the energy release rate from coating cracks [20]. Swain and Mencil [30] have suggested several reactions on nanoindentation load-depth curves as the fracture happened during nanoindentations at different arrangements of coating and the substrate. When a fracture occurred within the coating, the load–displacement curves perturbed (pop-in events), then the critical load for the pop-in incidents could be used to characterize the fracture toughness of a coating [12].

No study has been reported so far on the nanoindentation-induced delamination motivated by the crystallographic orientation of substrate in the film/substrate system. It has been experimentally shown that the deformation behavior of the single crystal of NiTi and NiTi/Ag is incredibly dependent on the crystallographic orientation [31]. The strengthening mechanism at the NiTi/Ag interface has been attributed to crystal orientation close to the substrate, causing discontinuous slip dislocation and high-loading/free-energy change for nanoindentation across the interface. Due to the complex nature of NiTi/Ag bilayers with the different crystallographic orientations of substrate, a comprehensive understanding of their plastic deformation is still a challenge and, therefore, it motivates the researchers toward the new topics. Until now, much effort has been made to show that a precise approximation of the free-energy difference ( $\Delta F$ ) by computational methods is essential to understand the details of the plastic deformation and strengthening mechanism which contribute to the thermodynamics and statistical mechanics to explain the non-equilibrium processes such as nanoindentation [32–34]. Although the Jarzynski’s equality has been developed to assess the free energy change during nanoindentation of the NiTi/Cu of different film thicknesses in a previous works [35], no report has been made yet on the free energy change of the bilayers along different crystallographic orientations under non-equilibrium conditions of the nanoindentation experiment.

This paper has three key goals: (i) Quantification of the role of the crystallographic orientation of the NiTi substrate on the dislocation emission process, that is, responsible for the irreversible plastic deformation of the NiTi/Ag bilayer. The obtained results will allow us to compare the atomistic details of the plasticity behavior of the six NiTi/Ag bilayers under nanoindentation load. The corresponding mechanical reply and dislocation density can then be examined. (ii) Analysis of the effect of the crystallographic orientation of NiTi substrate on the interfacial adhesion of the NiTi/Ag bilayers using the energy method. The average plastic dissipation can then be determined by a novel method developed for the cyclic nanoindentation tests, and an equivalently loaded clamped circular plate model will be adopted to evaluate the delaminated area. The Griffith energy balance will subsequently calculate the delamination energy release rate ( $G_{in}$ ). Accordingly, the changes of adhesion of the NiTi/Ag bilayers are investigated. (iii) Shedding some light on the effect of the crystallographic orientation of the NiTi substrate on the free energy change of the NiTi/Ag bilayers during the nanoindentation.

## 2. Computational work

Molecular dynamics simulation of the deposition and the nanoindentation models were performed by LAMMPS code [36]. Before the nanoindentation process, the sample of silver deposited on the equiatomic NiTi substrate was prepared. For deposition, the size of typical film/substrate was chosen to be rectangular simulation box with dimension of  $140 \times 140 \times 106 \text{ \AA}^3$ . The five bottom layers of the substrates are boundary atoms used to prevent the moving of the substrate by the incident atoms during deposition; subsequently, the upper ones could be considered as the thermostat layers. The motion of thermostat’s atoms follows the classical Newton’s second law, and thus these atoms could be called Newtonian atoms. The periodic boundary conditions (PBCs) were applied in X and Y directions, while free boundary condition is applied along the positive direction of Z. The timestep was 0.001 ps and the deposition is done by depositing one Ag atom every time step of 500 ps, meaning that the deposition rate is 2 atoms/ps. The temperature of atoms played as substrate are fixed to 400 K by Langevin thermostat [37]. The deposition takes place in a vacuum. Thus, the deposited Ag atoms are not coupled to the thermostat. Therefore, in the simulation, only the substrate atoms are connected to the thermostat. Langevin thermostat adds a random force to the particles, but does not perform time integration. This integration is done with the fix NVE ensemble. The Ag atoms are randomly deposited on the substrate. Each atom is located in the vacuum slab at a random position, from 6 to  $8 \text{ \AA}$  above the surface. A reflecting wall is placed at its top to prevent the atoms from leaving the simulation box in the deposition. During the deposition process of silver atoms, the system can experience a non-equilibrium state. The high energy of the deposited Ag atoms can be dissipated by Langevin thermostat in the progress of simulation to keep the whole temperature nearby 400 K (room temperature) corresponding to the value in the experiment [38]. Each simulation case proceeds until the 20,000 of Ag atoms are deposited on NiTi substrate and then a relaxation process of 1200 ps is conducted to enable the deposited thin film to be equilibrated. The primary configuration of the deposition model is visualized in Fig. 1.

After the deposition process, the NiTi/Ag bilayer system prepared was subjected to the cyclic-nanoindentation process. The indenter is considered as a virtual sphere with the radius of 3 nm and it was kept at a distance of about 1 nm over the modifying surface. During the nanoindentation process, the bottom layer ( $5 \text{ \AA}$ ) of the slab was fixed. The equations of motion were integrated using the Varlet algorithm with a time step of 0.002 ps.

Cyclic nanoindentation processes are conducted by controlling the indenter moving along the Z axis with a constant loading rate of  $5.0 \text{ ms}^{-1}$ . The maximum penetration depth in the present MD simulations was set at  $40 \text{ \AA}$  for each cycle. When the loading force reaches the

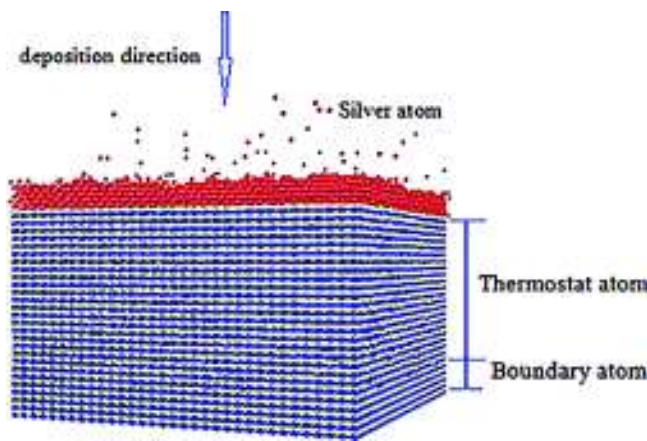


Fig. 1. Schematic illustration of Ag deposition on the NiTi substrate.

target force, the indenter will be kept at the position for relaxation before unloading. The unloading speed is the same with the loading speed. To study the response of NiTi/Ag bilayer to distinct cyclic loading rounds, three nanoindentations were performed on the same location. Each cycle was done at 400 K for 1600 ps using NVT ensemble where a Nose-Hoover thermostat was employed. This corresponds to a total simulation time of 4800 ps.

During the entire process, the interactions among Ag-Ni, Ag-Ti, and Ni-Ti are characterized by Embedded Atom Method (EAM) potential developed by Zhou et al. [39]. PBCs are imposed in the X and Y directions and the indenter axis was aligned with Z-axis. It is allowed to move in the negative Z-direction to indent on the top surface of the sample. The nanoindentation force exerted on the atoms is according to  $F(r) = -K(r-R)^2$  equation, where  $K$  is the force constant (set as  $10 \text{ eV}/\text{\AA}^3$  in this work),  $r$  is the distance from the atom to the axis of the indenter, and  $R$  is the radius of the indenter. The force is repulsive and set as 0 for  $r > R$ .

$$F = \begin{cases} -K(r-R)^2 & r < R \\ 0 & r \geq R \end{cases} \quad (1)$$

The sum of the nanoindentation forces on the atoms gives the indentation load in the load–displacement curves. To better understand the deformation process of NiTi/Ag bilayer under nanoindentation, the dislocation extraction algorithm (DXA) [40] was used to identify defects. Free software OVITO [41] is adopted to visualize the results.

### 3. Results and discussion

#### 3.1. Effect of crystallographic orientation of substrate on deformation mechanism of NiTi/Ag bilayers

Based on the previous experimental studies [42], deformation mechanism depends on the crystallographic orientation. The difference is due to the diverse slip-planes actuation simultaneously and accommodatingly at different crystallographic orientations [43]. However, experimental observations cannot explain the exact nature of the dislocations. Therefore, the MD simulation was performed to elucidate the mechanisms of the dislocation at different crystallographic orientations of the substrate. The force–depth curves obtained for the NiTi/Ag along a full nanoindentation and retraction cycle on the (100), (211), (321), (210), (010) and (111) faces of the NiTi are presented in Fig. 2. Nucleation, propagation and annihilation of the dislocations in the NiTi/Ag bilayers underneath the nanoindentation pin are responsible for the mechanisms of diverse plastic deformation. We found in all NiTi/Ag bilayers that, the crystallographic orientation of the NiTi substrate affects the load of nanoindentation as well as the mechanism

of plastic deformation. It must be emphasized that, although the representative discontinuities are exhibited in all load–depth nanoindentation curves on the bilayers at the different crystallographic orientations, they are caused by the dissimilar dislocation events, meaning that there exist diverse initial mechanisms of plastic deformation. As the quantity of dislocations is increased by growing loading, they start to entangle with each other. This could provide an effective dislocation pinning, in turn, hindering dislocation propagations [44].

To elucidate the deformation mechanism versus depth, the chosen points a ( $h = 20.5 \text{ \AA}$ ), b ( $h = 23.8 \text{ \AA}$ ), c ( $h = 26.4 \text{ \AA}$ ), d ( $h = 34.1 \text{ \AA}$ ) and ( $e = 37 \text{ \AA}$ ) of the NiTi (100)/Ag were illustrated in Fig. 3. Fig. 4 shows the atomistic schematics of the NiTi (100)/Ag at points a, b, c, d, and e. We encourage the reader to also look at the profile energies of the dislocations of the NiTi (100)/Ag at mentioned points, provides as supplementary data. At the beginning of the nanoindentation  $P$  was positive ( $h = 0$ ), which attributed to the repulsion among the indenter and NiTi/Ag bilayer atoms, when the distance between atoms is smaller than that of equilibrium one [45,46]. At the depth of  $h < \sim 12 \text{ \AA}$ , the deformation happened in the contact region between indenter and sample is elastic. In the depth of  $12 \text{ \AA} \leq d \leq 20.5 \text{ \AA}$ , some slight fluctuations were observed, corresponding to the plastic deformation of Ag film layer. At the point a ( $h = 20.5 \text{ \AA}$ ) the primary transition from elastic to plastic deformation of NiTi substrate (pop-in event) is occurred. This transition is consistent with the simulation results of Lilleodden et al. [47], Lee [48] and Fu et al. [49]. Notice that the multiple pop-ins exposed through the current bilayer are comparable to that realized previously in other multilayers with different crystal structures of the substrate. Li et al. [50] have suggested that the dislocation nucleation could soften the materials, e.g. as the Cu/Ni nanotwinned multilayer films underneath the cylindrical indentation region [45]. As seen in Fig. 3, the  $P$ - $h$  curve displays a constant ascending tendency with no distinguished drop between the points a and b, as it has been similarly seen in the nanoindentation of the Ag/Ni multilayer films of a spherical indenter [51]. At the primary defect-nucleation step, plasticity grows as the balance between two renowned distinctive mechanisms: twinning and dislocation; as reported before [52]. As the depth increases, further dislocations are nucleated and propagated, encouraging the drop of stress and release of the strain energy. In the depth of  $h > 26.4 \text{ \AA}$ , the load–depth curve follows a zigzag way. This behavior is due to the production of more nucleation of dislocations in different directions and interactions, of which it appears a nest-like arrangement of twins, as seen in Fig. 4. In the depth of  $26.4 \text{ \AA}$ , more dislocations with different energies are appeared, and stacking faults by  $b = \langle 100 \rangle$  are increased in size and energy. In the range  $34.1 \text{ \AA} \leq d \leq 37 \text{ \AA}$ , the dislocations can quickly transfer to the side of the bilayer and destroy at the free surface; releasing stress and leading to an obvious drop in force (Fig. 3). The portion between points d and e is nearly flat, suggesting the softening of the material. This distinct softening should chiefly attribute to the creation of partial twinning slips [53].

Deformation mechanism of the bilayers at NiTi (321) or (210) facet is similar to that of NiTi (100)/Ag face. In these cases, the load–depth curves primarily have an analogous profile. The pop-in event occurs at depth of  $\sim 20 \text{ \AA}$  with the burger vector  $b = 1/2 \langle 1-11 \rangle$  and  $b = \langle 100 \rangle$  in the NiTi/Ag as NiTi aligned at (321) and (210) faces, respectively (Fig. 5a and b). In both samples of bilayers, the next big drop in force happens at  $h \sim 23 \text{ \AA}$ . Note that, in this depth, multiple dislocations with different burger vectors including  $b = \langle 001 \rangle$ ,  $1/2 \langle -1-1-1 \rangle$ ,  $1/2 \langle 11-1 \rangle$ ,  $1/2 \langle 1-11 \rangle$  and  $1/2 \langle -111 \rangle$  could be appeared under the area of the indentation of the NiTi (321)/Ag. The plastic deformation of NiTi (210)/Ag is due to the creation of a major dislocation with  $b = \langle 100 \rangle$  (Fig. 5c and d).

Similar to NiTi (100)/Ag, profuse twinning is produced in the early stages of plasticity, and as the indenter continues penetrating, the interaction of twins creates a nest-like organization of twins [52]. In both cases, located at  $h \sim 27 \text{ \AA}$ , there is one major mixed dislocation with

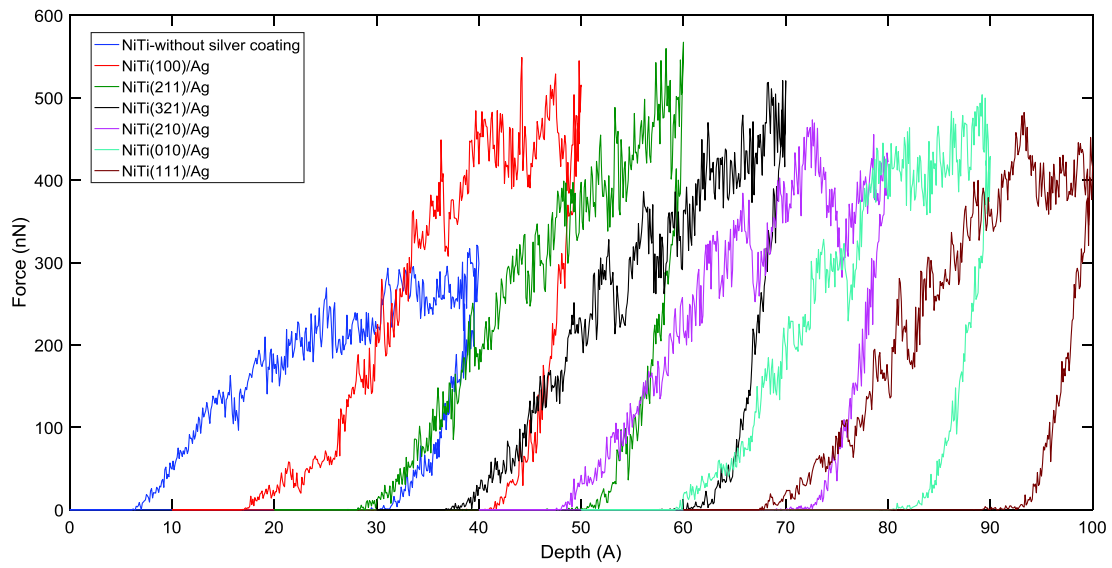


Fig. 2. Force-depth curves of the NiTi without silver coating and NiTi/Ag bilayer having different crystallographic orientations at depth of 40 Å. Look at the respective shifting of the curves for (1 0 0), (2 1 1), (3 2 1), (2 1 0), (0 1 0) and (1 1 1) faces to the right by 10, 20, 30, 40, 50 and 60 units.

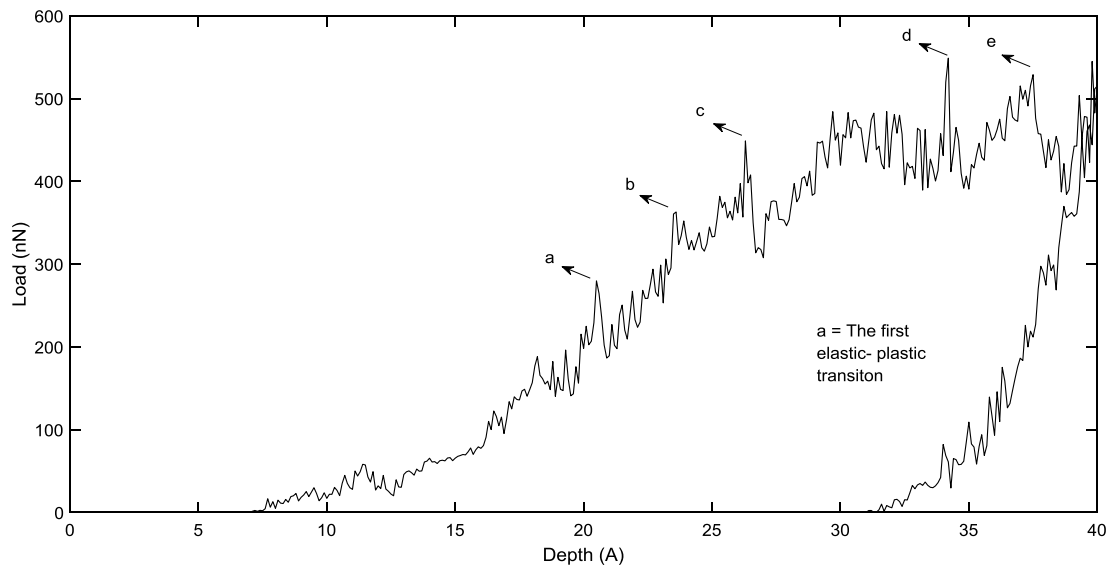


Fig. 3. The nanoindentation load-depth curve for the NiTi (1 0 0)/Ag bilayer.

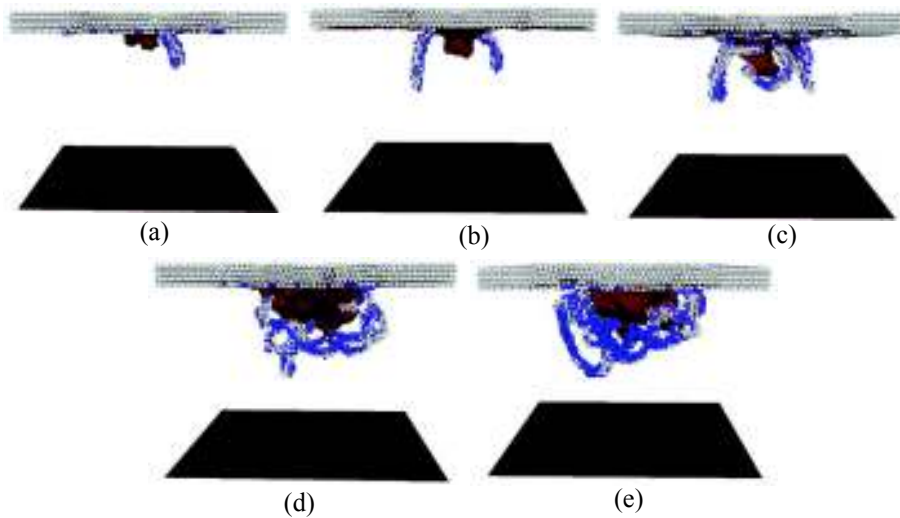
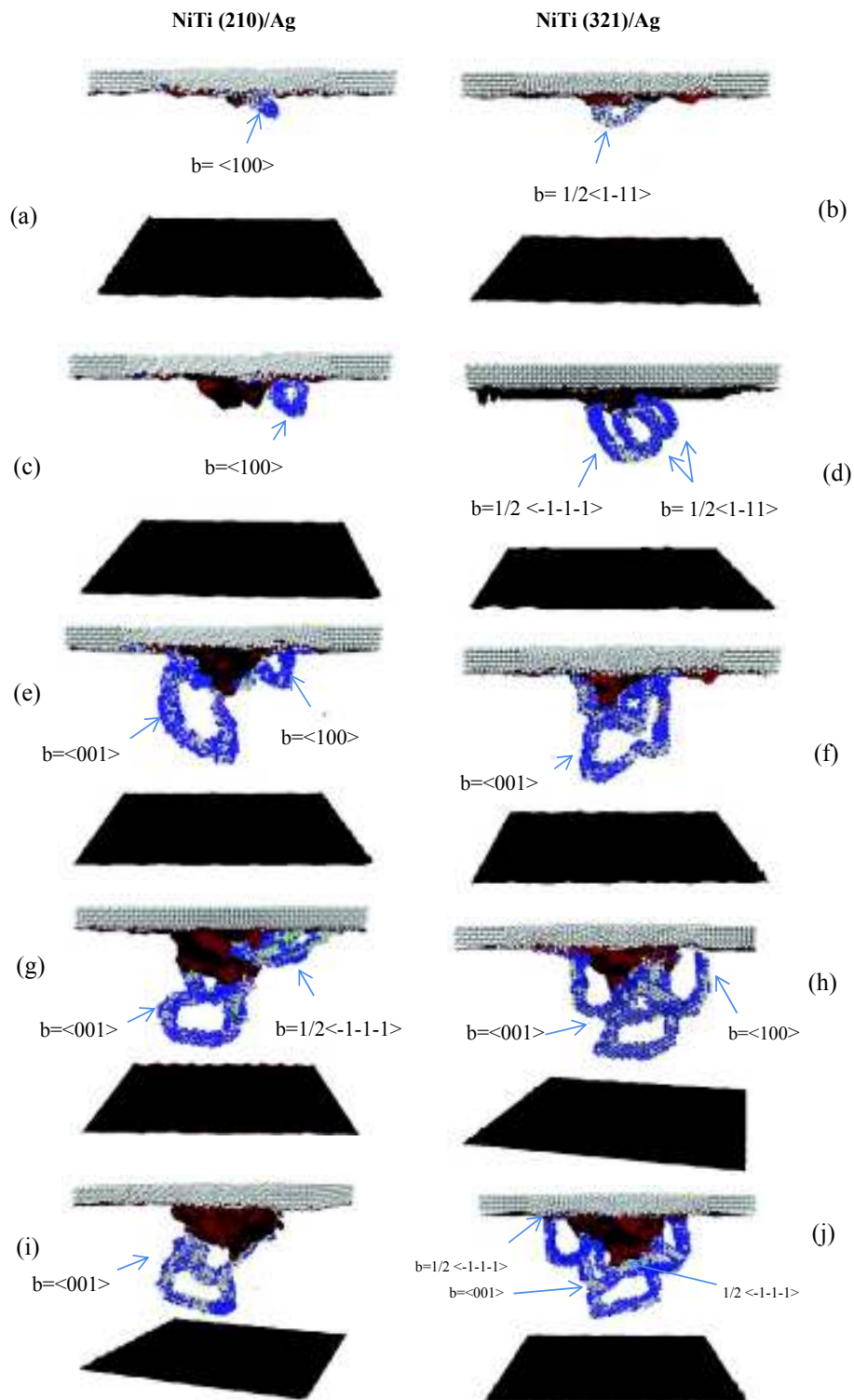


Fig. 4. Atomistic schematics of the NiTi (1 0 0)/Ag bilayer at points a, b, c, d, and e corresponding to depth of  $h = 20.5 \text{ \AA}$ ,  $23.8 \text{ \AA}$ ,  $26.4 \text{ \AA}$ ,  $34.1 \text{ \AA}$  and  $37 \text{ \AA}$ , respectively.



**Fig. 5.** Atomistic schematics of NiTi (210)/Ag and NiTi (321)/Ag dislocations in the depth of (a) and (b) = 20Å, (c) and (d) = 27Å, (e) and (f) = 32Å, (g) and (h) = 35Å, (i) and (j) = 37Å, respectively.

burger vector of  $b = \langle 001 \rangle$ , at the center of the spherical central region, causing a significant drop in the load. The mixed dislocation of NiTi (321)/Ag is longer than that of NiTi (210)/Ag (Fig. 5e and d). Both bilayers have similar trends in the range of  $27 \leq h \leq 32 \text{ \AA}$ , and the nanoindentation force continues to higher values (Fig. 2). This increase is due to the interaction of the dislocations with each other and nucleation of them which follows gliding continually. But two new dislocations with burger vector of  $b = 1/2 \langle -1, -1, -1 \rangle$  are

observed around the surface in the case of NiTi (210)/Ag, where wedges of the atoms move down to the right side of the bilayer, leading to a major drop in the load at  $h \sim 35 \text{ \AA}$  (Fig. 5g). However, the mentioned dislocations are annihilated at  $h \sim 37 \text{ \AA}$  (Fig. 5i). Also, various partial dislocations of both cases nucleate and move in the range of  $37 < h \leq 40 \text{ \AA}$  (Fig. 5i and j). However, the plastic deformation mechanism of NiTi (321)/Ag needs to interact with number of the dislocations, as compared to the deformation mechanism of NiTi (210)/

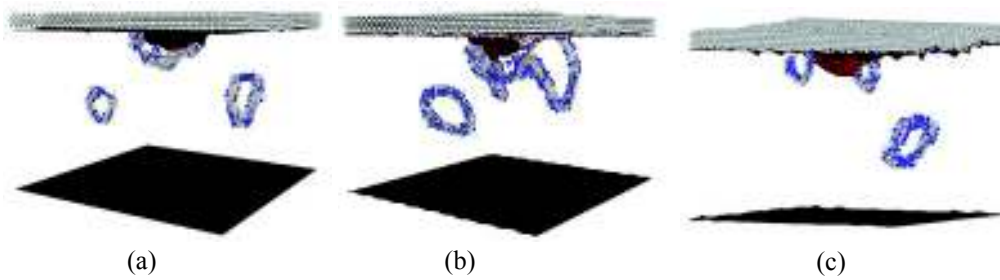


Fig. 6. The atomistic schematics of the initial full dislocation loop formation at depth of 25 Å, 27 Å and 25 Å in the cases of NiTi (0 1 0)/Ag, NiTi (1 1 1)/Ag and NiTi (2 1 1)/Ag, respectively.

Ag. This behavior is responsible for the forces on the NiTi (3 2 1)/Ag, which is considerably superior to the NiTi (2 1 0)/Ag for indentation depths of  $36 < h \leq 40$  Å. The atomistic schematic of the bilayers as NiTi aligned at (3 2 1) and (2 1 0) facets in the depth of 40 Å is shown in Fig. 9.

The nanoindentations on NiTi (0 1 0)/Ag, NiTi (1 1 1)/Ag and NiTi (2 1 1)/Ag have similar plastic responses, which are controlled by dislocation nucleation and formation of a prismatic loop. The initial dislocation under the area of indentation happens around  $h \sim 20$  Å in all three cases. As seen, various partial dislocation loops are observable at  $20 \leq h \leq 25$  beneath the indentation. The initial dislocation loop is released towards the bottom of the bilayers at  $h = 25$  Å, 25 Å and 27 Å for the cases of NiTi (2 1 1)/Ag, NiTi (0 1 0)/Ag and NiTi (1 1 1)/Ag, respectively (Fig. 6). It is notable that, the profile of energies for the initial dislocation loop formation of three mentioned cases is presented in Fig. S2. At these cases, respectively, one ( $b = \langle 00\bar{1} \rangle$ ), two ( $b = \langle 001 \rangle$ ,  $b = \langle 0\bar{1}0 \rangle$ ) and one ( $b = \langle 001 \rangle$ ) mixed dislocation loops are released. Further, more noticeable dislocations with different burger vectors are formed around the tip for these cases. In the case of NiTi (2 1 1)/Ag, more dislocations are nucleated toward the left side of the bilayer as the indenter descends further, while the previous dislocation ( $b = \langle 00\bar{1} \rangle$ ) loop released is sustained at the other side of the bilayer (Fig. 7b). At  $25 \leq h \leq 40$  Å, more nucleation dislocations hit the left side of the bilayer. These dislocations are appeared to have a mixed character burger vector (parallel-to-the surface). No nucleation of new defects on the other side of the bilayer is detected, even at the maximum indentation force of 570.3 nN (Figs. 7d and 9c).

In the case of NiTi (0 1 0)/Ag, when  $26 \leq h \leq 33$  Å, the dislocation loops with  $b = \langle 001 \rangle$  and  $b = \langle 0\bar{1}0 \rangle$  move to the right side and glide down to the left side of the bilayer, respectively (Fig. 7a). However, new dislocations continue to nucleate under the indentation pit at this range of depth. At  $h \sim 34$  Å, a new dislocation emerges with a mixed character and a burger vector ( $b = \langle 0\bar{1}0 \rangle$ ) perpendicular to the surface. The propagation of this dislocation produces a visible pure edge character deformation around the indenter at  $h \sim 37$  Å. When  $h \sim 38$  Å, a dislocation loop with burger vector of  $b = \langle 010 \rangle$ , parallel to the surface is released (Fig. 7b). The partial dislocations interact with this dislocation loop to push it to the left side of the bilayer at  $39 < h < 40$  Å. In the case of NiTi (1 1 1)/Ag, (Fig. 8), growth of the dislocation with  $b = \langle 0\bar{1}0 \rangle$  and emission a prismatic loop with burger vector  $b = \langle 010 \rangle$  toward the right side of the bilayer at  $27 \leq h \leq 31$  Å may be causing a significant drop in the load (Fig. 8a). It should be noted that Hagelaar et al. [54] have also observed the formation of the prismatic loop during loading of the nanoindentation for the (1 1 1) face. In the range of  $34 \leq h \leq 40$  Å, different dislocations can nucleate continuously; some of them quickly move to both sides of the substrate and remain there, while others move to the free surface and then annihilate (Fig. 8b).

In summary, all bilayers are displayed extensive plastic regime for nanoindentation depth underneath  $20 < h < 40$  Å. Depending on the crystallographic orientation of the substrate, different deformation mechanisms of the bilayers under load were studied. Fig. 9 illustrates the plastic deformation mechanisms of all bilayers at maximum indentation depth. Prismatic dislocation loop and nest-like organization

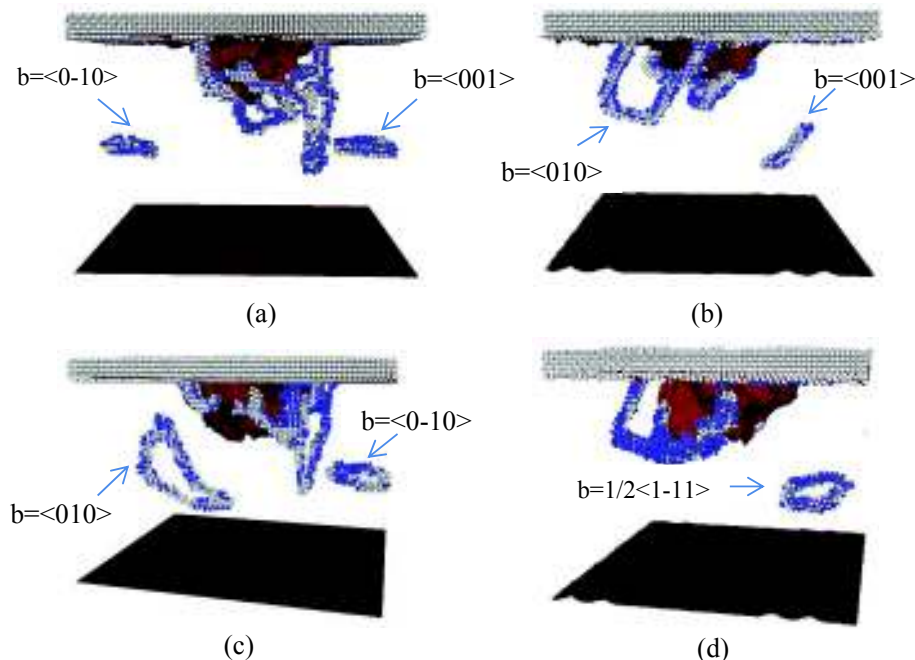


Fig. 7. The Atomistic Schematic of dislocations of (a) NiTi (0 1 0)/Ag and (b) NiTi (2 1 1)/Ag at  $h = 33$  Å, (c) NiTi (0 1 0)/Ag and (d) NiTi (2 1 1)/Ag at  $h = 38$  Å.

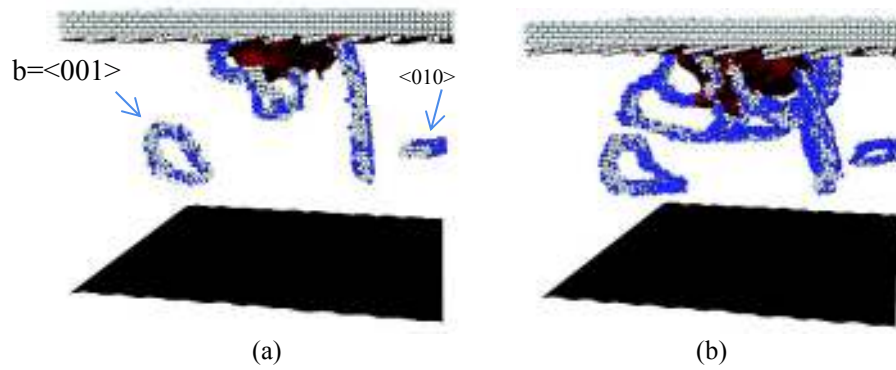


Fig. 8. The Atomistic Schematic of NiTi (1 1 1)/Ag dislocations at (a):  $h = 31 \text{ \AA}$  and (b):  $h = 37 \text{ \AA}$ .

of twins can be considered responsible for the plastic conveyance of the bilayers in the cases of (211,010,111) and (100,210,321), respectively. These clarifications of dissimilarities in deformation mechanisms of the NiTi/Ag bilayers can help to describe the difference of the dislocation densities measured for each type of crystallographic orientation as discussed in the next section.

### 3.2. Hardness and reduced Young's modulus of the NiTi/Ag bilayer

Precise estimation of hardness and elastic modulus of a thin film requires careful evaluation of all parameters. The nanoindentation force rises with the depth due to contact-area growth, even if no softening or strengthening is considered. The Oliver-Pharr method is applied [5,14,55,56] to estimate the Hardness of the NiTi/Ag bilayer with different crystallographic orientations of the NiTi, from the loading force-depth curves. The hardness  $H$ , which is defined as the ratio of maximum applied load ( $P_{\max}$ ) to the projected contact area  $A$ , i.e.,  $H = P_{\max}/A$ , where  $A = \pi(2R-h_c)h_c$  with  $R$  and  $h_c$  the indenter radius and contact depth of the spherical nanoindentation, respectively. The  $P_{\max}$ , the slope of the initial portion of the unloading curve ( $S$ ) and the contact depth of the spherical nanoindentation ( $h_c$ ) are the desirable parameters that are calculated from the nanoindentation load–displacement graph and tabulated in Table 1. It should be noted that;  $h_c$  can be calculated by the Oliver-Pharr method as follow:

$$h_c = h_{\max} - 0.72 \frac{P_{\max}}{S_{\max}} \quad (2)$$

Table 1

Slope of the initial portion of the unloading curve ( $S$ ), the maximum applied load ( $P_{\max}$ ), the contact depth of the spherical indent ( $h_c$ ), Hardness and Reduced Young's modulus calculated for the NiTi/Ag bilayer at different crystallographic orientations at the maximum indentation depth ( $h = 40 \text{ \AA}$ ).

NiTi/Ag bilayer	$S$	$h_c$ ( $\text{\AA}$ )	$P_{\max}$ (nN)	Hardness (GPa)	Reduced Young's modulus (GPa)
NiTi(2 1 1)/Ag	63.26	35.63	567.33	22.58	81.564
NiTi(3 2 1)/Ag	85.54	36.23	520.53	20.72	81.569
NiTi(1 0 0)/Ag	85.44	36.14	515.25	20.03	81.568
NiTi(2 1 0)/Ag	71.50	35.65	422.35	17.06	81.564
NiTi(1 1 1)/Ag	78.55	36.35	428.79	16.81	81.570
NiTi(0 1 0)/Ag	77.17	35.60	415.76	16.55	81.563
NiTi-without the silver coating	56.33	36.17	298.96	11.90	73.12

According to the literature, if the numerical values for the  $\frac{h_f}{h_{\max}}$  ratio are greater than 0.7, the values of hardness would overestimate from loading–unloading plots based on the Oliver and Pharr method. It is notable that  $h_f$  is the final indentation depth of the impression after unloading. According to the obtained results, the  $\frac{h_f}{h_{\max}}$  ratio for the six cases of bilayers is observed to be higher than 0.7, that are, 0.75, 0.76, 0.75, 0.75, 0.76 and 0.76, as NiTi aligned at (1 0 0), (0 1 0), (1 1 1), (2 1 1), (2 1 0) and (3 2 1) faces, respectively. In order to consider both film and substrate effects, a solution of Saha and Nix [57,58] is used to

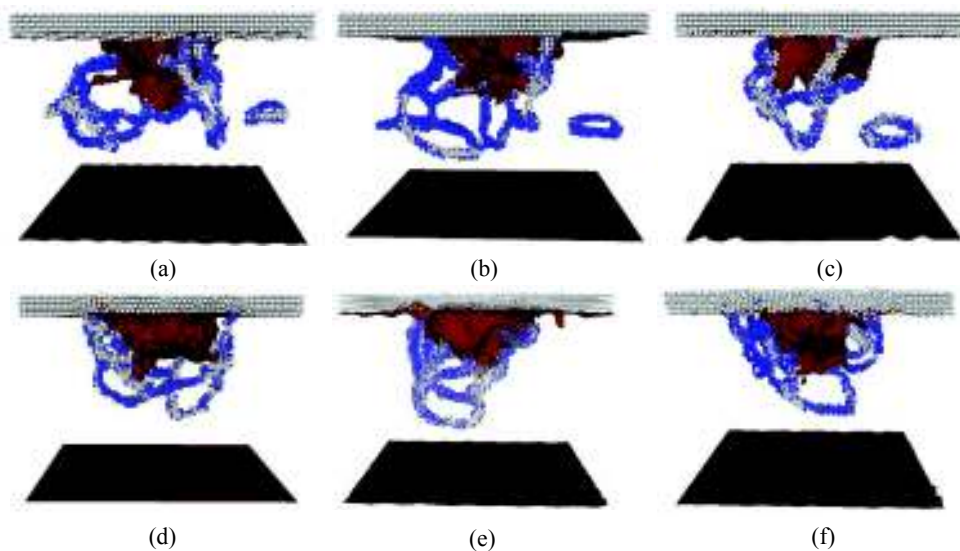


Fig. 9. Plastic deformation mechanisms of (a) NiTi (1 1 1)/Ag, (b) NiTi (0 1 0)/Ag, (c) NiTi (2 1 1)/Ag, (d) NiTi (1 0 0)/Ag, (e) NiTi (2 1 0)/Ag and (f) NiTi (3 2 1)/Ag bilayers at maximum indentation depth ( $h = 40 \text{ \AA}$ ).

estimate the reduced Young's modulus which takes account of both film and substrate for elastic–plastic response in the case of bilayer systems. An empirical equation which could be expressed the connection between the reduced modulus and the indentation depth has been suggested by this model. So it is common to define it as:

$$\frac{1}{E_r} = \frac{1 - \nu_f^2}{E_f} \left(1 - e^{-\frac{\alpha d}{hc}}\right) + \frac{1 - \nu_s^2}{E_s} e^{-\frac{\alpha d}{hc}} + \frac{1 - \nu_i^2}{E_i} \quad (3)$$

where  $d$  is the film-thickness, and  $\alpha = 0.25$  is an empirical parameter attained via fitting a series of nanoindentation results.  $E_f$  and  $\nu_f$  are the modulus and Poisson's ratio of the film,  $E_s$  and  $\nu_s$  are these quantities for the substrate, respectively. The values of reduced Young's modulus and Hardness of the NiTi/Ag bilayers and NiTi without the silver coating, for the same penetration depth are listed in Table 1. As seen in Table 1, the reduced Young's moduli for all bilayers are found to be the same and larger than that of NiTi without a silver coating. But, the measured hardness decreases in the following trend: NiTi (2 1 1) > NiTi (3 2 1) > NiTi (1 0 0) > NiTi (2 1 0) > NiTi (1 1 1) > NiTi (0 1 0) > NiTi with no coating of the silver. Thus, it can be concluded that the mechanical behavior of the equiatomic NiTi alloy can be improved by deposition of the silver atoms on it and consequently, the NiTi/Ag bi-layer can be suitable for engineering and medical applications. It is also consistent with the load-depth curve of the NiTi/Ag bilayers and the NiTi without the silver coating (Fig. 2). More importantly, hardness is found to increase with increasing of the dislocation density at the maximum depth of indentation ( $h = 40 \text{ \AA}$ ). The calculation of dislocation density induced by the nanoindentation of all bilayers is discussed in the next section.

### 3.3. Dislocation density

Dislocation density in either a bilayer or multilayer material has been analyzed due to a high concern for several years, as dislocations are closely related to the plastic deformation, and consequently have a deep effect on mechanical properties of any material [59]. Dislocation density is an essential input of several hardening systems, e.g., the renowned Taylor model [60]. In this section, it is revealed that the dislocation density can be calculated by the information gathered from the atomistic structure, corresponding to the geometrically necessary dislocations (GNDs) [61]. This model assumes that the GNDs encouraged by pressing the indenter into the material is forced to the nearly spherical volume under the region of contact [62]. It should be noted that the indented surface is essentially smaller than the radius of the plastic zone, due to the fact that GNDs of analogous sign gathered in the indented volume, will effectively repel each other. Consequently, growth of the plastically distorted volume, as proposed by Durst et al. [63], is the largest. Dislocation density in the plastic zone is defined by the total length of all dislocation segments per unit volume:

$$\rho = \frac{L_d}{V_p} \quad (4)$$

The plastic zone volume can be calculated from the correlation described in the literature [63,64]:

$$V_p = \frac{2}{3} \pi R_p^3 - V_{ind} \quad (5)$$

where  $R_p$  is the radius of the plastic zone and  $V_{ind} = \pi h^2 (R-h)/3$  is the imprint volume of the indenter. It is notable that,  $R$  and  $h$  are the indenter radius and penetration depth, respectively. Fig. 10 displays a schematic drawing for estimation of the dislocation density under the indent, where  $a_c$  is the radius of the projected area [65]:

$$a_c = \sqrt{(R^2 - (R-h)^2)} \quad (6)$$

In our simulation,  $a_c$  is  $\sim 30 \text{ \AA}$ , and the length of the lines can be achieved by DXA.

The results show clearly that both the dislocation density induced

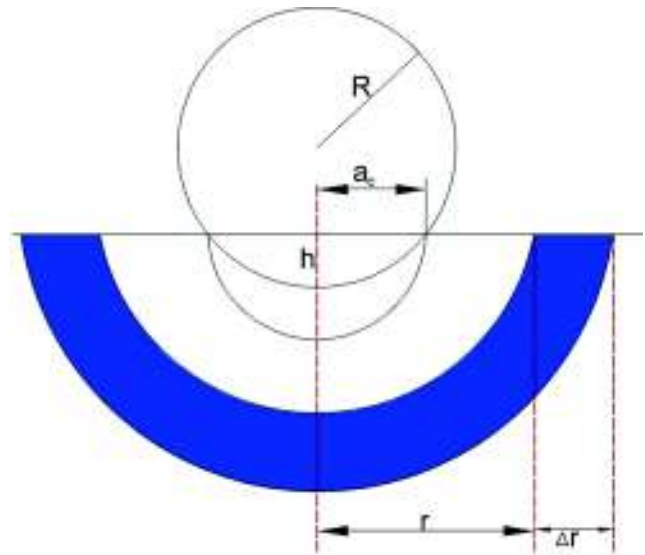


Fig. 10. Schematic drawing to evaluate the dislocation density.

by nanoindentation and change with the depth of the indented region are depended to the crystallographic orientation of the substrate. These results are in good agreement with the experimental results achieved by Chiu et al. [66]. Fig. 11 shows the dislocation density versus depth for samples deformed by the indenter. The increase in the dislocation density with depth is expectable, but clarification can be made by generation and propagation of the dislocations during the deformation of the bilayers. On the other hand, the dislocation density of all bilayers firstly reaches the maximum value at a depth of  $\sim 33 \text{ \AA}$ , and then decreases again when the value of depth goes up. The repulsive interactions among the dislocations can lead to saturation of the dislocation density at the depth of  $40 \text{ \AA}$ . After saturation of the supplied dislocations, the propagation of the dislocations can occur by more deformation, but the dislocation density should retain constant via the balanced generation and annihilation of the dislocations.

As mentioned in section 3.1, prismatic dislocation loop and nest-like organization of twins were found to be responsible for the irreversible deformation of plastic at the bilayers in the cases of (211,010,111) and (100,210,321), respectively. These processes are consequent of the type of dislocation mechanism, shape distortion and subsequent different density dislocation value under the plastic zone [38]. The average dislocation densities of all bilayers created by radius of  $30 \text{ \AA}$  at the indentation depth of  $h = 33 \text{ \AA}$  and  $40 \text{ \AA}$  are presented in Table 2. The results show that the dislocation density induced by nanoindentation of NiTi (0 1 0)/Ag at  $h = 33 \text{ \AA}$  was somewhat higher than that of other bilayers. The growth process of dislocation loop may shed light on why the dislocation density of NiTi (0 1 0)/Ag is higher than that of other orientations. As discussed above, in the range  $26 \leq h \leq 33 \text{ \AA}$ , two dislocation loops could shift the sides of the substrate and lead to the high aggregation of dislocations in the plastic zone. It can be concluded that, although the dislocation density is maximum in all bilayers at depth =  $33 \text{ \AA}$ , densification is occurred for a higher value of equivalent depth in the case of bilayers deformed by mechanisms of loop formation.

In order to confirm the obtained results of density dislocation of bilayers under the indenter at depth =  $33 \text{ \AA}$ , the variation in the von Mises stress in the atomic framework is investigated for all bilayers. The evolution of Von Mises stress of bilayers can be a valuable criterion to detect the plastic deformation and intensity of density dislocation under nanoindentation. Fig. 12 displays the cross-section views of residual Von Mises stress distribution with six different orientation surfaces of the substrate at the same indentation depth ( $h = 33 \text{ \AA}$ ). The significant differences in the von-Mises stress could be attributed to the difference

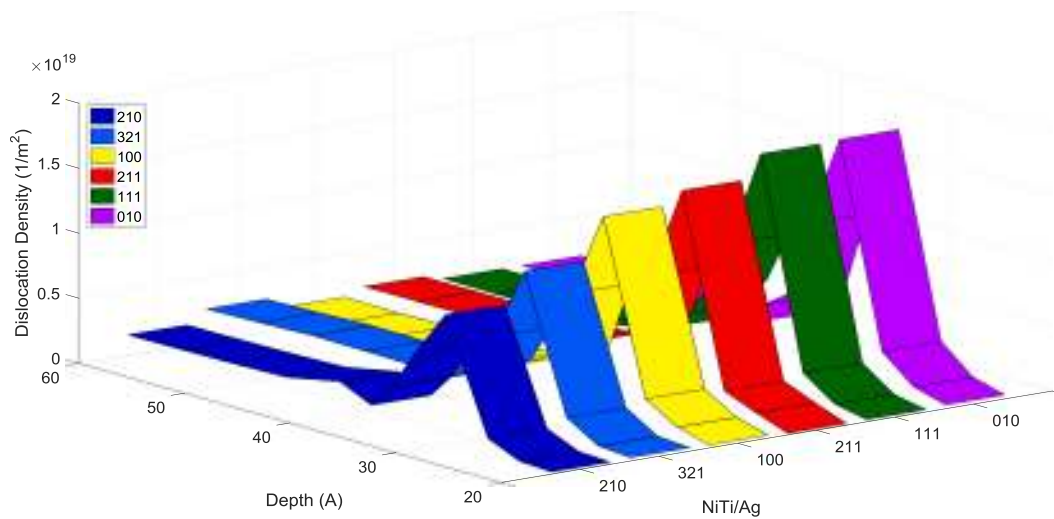


Fig. 11. Graph of density dislocation versus depth for NiTi/Ag bilayers deformed by indenter at the depth of 33 Å.

Table 2

Dislocation density induced by the nanoindentation of all bilayers at depths = 33 Å and 40 Å.

NiTi/Ag bilayers	Dislocation Density at depth of 33 Å (m <sup>-2</sup> )	Dislocation Density at depth of 40 Å (m <sup>-2</sup> )
NiTi(0 1 0)/Ag	1.84 × 10 <sup>19</sup>	1.84 × 10 <sup>18</sup>
NiTi(1 1 1)/Ag	1.82 × 10 <sup>19</sup>	1.96 × 10 <sup>18</sup>
NiTi(2 1 1)/Ag	1.64 × 10 <sup>19</sup>	2.66 × 10 <sup>18</sup>
NiTi(1 0 0)/Ag	1.55 × 10 <sup>19</sup>	2.49 × 10 <sup>18</sup>
NiTi(3 2 1)/Ag	1.23 × 10 <sup>19</sup>	2.57 × 10 <sup>18</sup>
NiTi(2 1 0)/Ag	1.21 × 10 <sup>19</sup>	2.03 × 10 <sup>18</sup>

prismatic formed in the NiTi/Ag bilayer as NiTi aligned at (0 1 0), (1 1 1) and (2 1 1) faces. The average stress of NiTi (0 1 0)/Ag under indenter is considerably higher than that of other surrounding samples. The reasons for this behavior are probably comparable with those previously reported in the subject of the dislocation density, where it has been considered as the relation between dislocation density and deformation process at the same equivalent depth.

Fig. 13 shows the relationship between density dislocation and hardness of the bilayer at h = 40 Å. As seen, the dislocation density induced by the nanoindentation of the bilayers at a maximum depth of h = 40 Å increases when the hardness of the bilayer comes up. When a bilayer is plastically deformed, the dislocation density is increased, leading to strain hardening [67], by the increase of the density of the bilayer dislocation. Thus, the available space under the indenter for dislocations movement will be limited, then, hardness increases.

between dislocation densities among the six kinds of bilayers. It is worthy to note that higher dislocation density at the same indentation depth leads to the higher von Mises stress distribution. It can be seen from this Fig that the Von Misses stress field is more focused on the loop

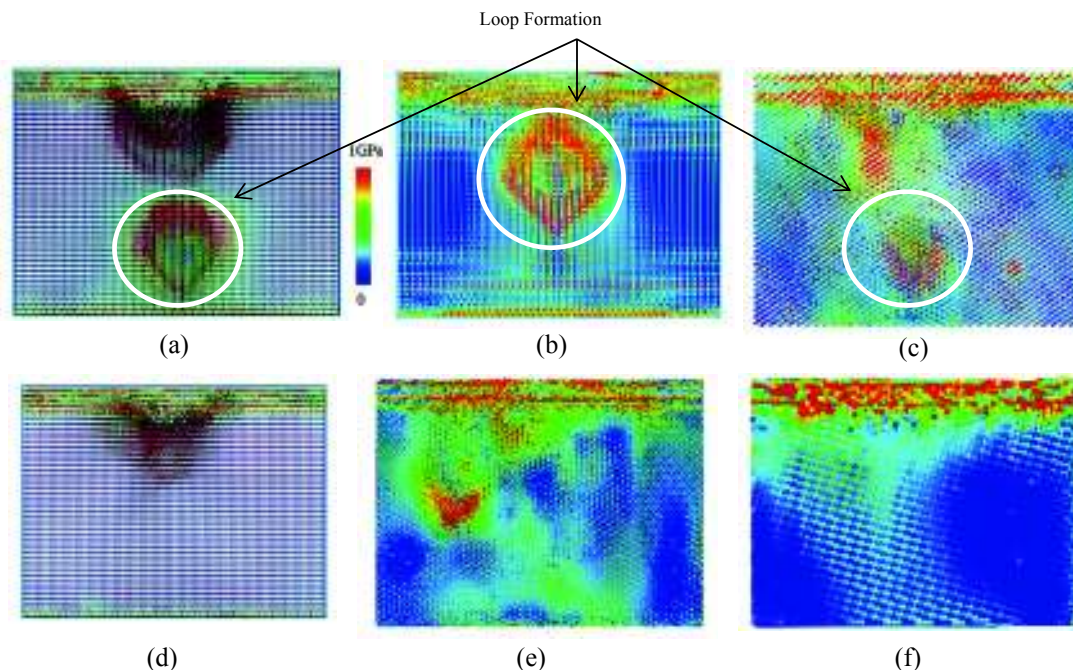


Fig. 12. The cross-section views of residual Von Mises stress distribution of (a) NiTi(0 1 0)/Ag, (b) NiTi(1 1 1), (c) NiTi(2 1 1), (d) NiTi(1 0 0)/Ag (e) NiTi(3 2 1)/Ag and (f) NiTi(2 1 0)/Ag at the same indentation depth (h = 33 Å).

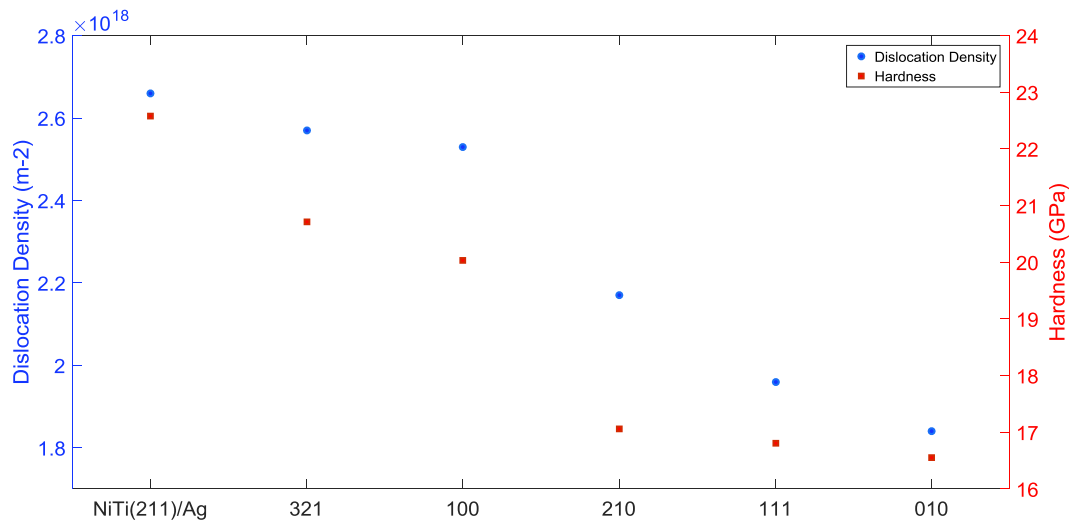


Fig. 13. Dislocation density and Hardness of the NiTi/Ag bilayers with the different crystallographic orientations of the substrate.

### 3.4. Cyclic nanoindentation

In order to discuss the elastic/plastic deformation of the bilayer in more details, the cyclic nanoindentation test was applied to the bilayer system. Under the cyclic loading, the indenter was continued to move into the materials as similar as the creep deformation of the materials. Similar to single nanoindentation, undesirable dislocations are released from the sources during the unloading, while excess dislocations are produced in the loading phase. It is important to note that, according to our investigation described in section 3.1, the behavior of the bilayers is more complicated than that of assumed here and strongly depends on the crystallographic orientation of the substrate. Therefore, it is known that the estimations of the plastic energy dissipation in each loading–unloading cycle require careful assessment of the parameters.

Cyclic nanoindentation tests were performed on a NiTi/Ag bilayer with a maximum indentation depth of 40 Å for each cycle. The Load–Time curve of NiTi/Ag bilayer is plotted in Fig. 14, to indicate the sequence of indentation and response of NiTi/Ag bilayer during the multi-step loading–unloading process. It is clear from Fig. 14, at maximum depth; the nanoindentation force is higher in the first loading cycle, lower in the second loading cycle and the lowest in the third cycle. This effect shows that the maximum force decreases with the increase of the

loading–unloading cycle. When the indenter moves into the NiTi/Ag, it causes deformation in the bilayer. Once the bilayer is unloaded, the elastic and adhesive forces start to recover in the vicinity of the indenter. Due to the distorted structure, the recovery forces are not as major as before. Hence the resistance to the second loading cycle is lower than the first one, and so is for the third loading – unloading cycle and vice versa. It shows that the defects and deformations produced after each indentation cycle are responsible for the decrease of the adhesive recovery forces. Further, an increase in the number of indentation cycles can reduce the maximum indentation force, under the condition of constant depth.

It is generally agreed from the single nanoindentation simulation that, the shakedown phenomenon might occur using the indentation with small amplitude of the indentation load. The cyclic nanoindentation is then controlled by the elastic deformation, and no dislocation is emitted from the edge of the contact zone during the loading–unloading cycle.

The plastic energy dissipated in each loading–unloading cycle ( $E_{plastic}$ ) can be calculated as [68]:

$$E_{plastic} = E_{loading} - E_{unloading} = \int_{loading} Fd\delta - \int_{unloading} Fd\delta \quad (7)$$

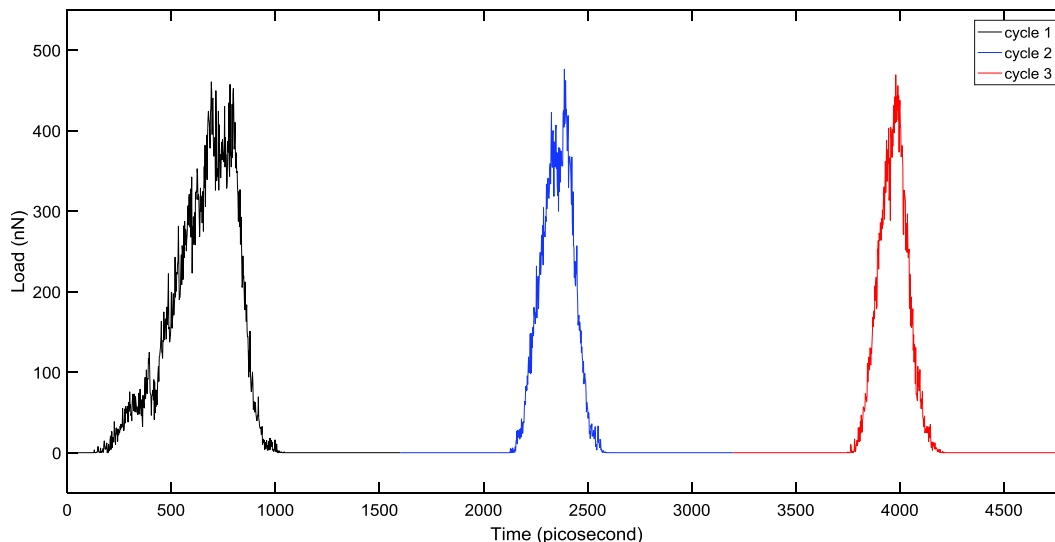
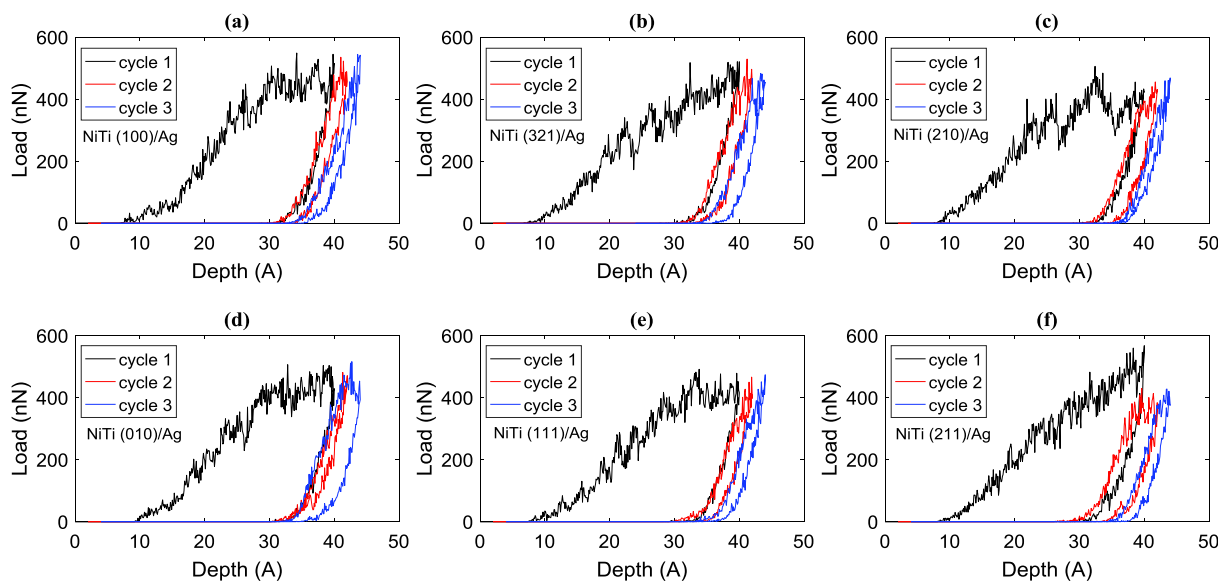


Fig. 14. The schematic of cyclic nanoindentation process of NiTi/Ag bilayer.



**Fig. 15.** Typical loading–unloading curves at the cycles 1, 2 and 3 cycles for the cyclic nanoindentation under 400 nN average load and indentation frequency of 0.5 cycle/s for the NiTi/Ag bilayer at different crystallographic orientations of the NiTi. Note: Curves of cycles 1 and 2 are shifted 2 and 4 unit to the right in all diagrams, respectively.

which is the area enclosed by the loading–unloading curve.

Fig. 15 shows the loading–unloading curves at the cycles 1, 2 and 3. Accordingly, the average plastic energy dissipated per cycle in the cyclic nanoindentation can be considered as [68]:

$$E_{\text{plastic}} = \frac{1}{n_{\text{max}}} \sum_{n=1}^{n_{\text{max}}} E_{\text{plastic}}^{\text{max}} \quad (8)$$

where  $n_{\text{max}}$  is the maximum indentation cycle carried out in the cyclic nanoindentation test.

The results of  $E_{\text{plastic}}$  obtained for all bilayers with the different crystallographic orientations of NiTi are reported in Table 3. The results are in good agreement with those obtained from Section 3.5, and evidently, demonstrate that the NiTi (2 1 1)/Ag bilayer exhibits a lower  $E_{\text{plastic}}$ .

Less energy is dissipated for severely deformed NiTi (2 1 1)/Ag due to having a higher hardness (at the maximum depth of indentation,  $h = 40 \text{ \AA}$ ) compared to the more dissipated energy of NiTi (0 1 0)/Ag bilayer. In the case of NiTi (0 1 0)/Ag bilayer with the lower hardness, the more plasticity is occurred, leading to the more dissipated plastic energy in each indentation cycle. The details of interfacial toughness of bilayers and its relation to the plastic energy will be discussed in the next section.

### 3.5. Indentation-induced interfacial delamination mechanics

The observations specify that delamination is the result of an intricate interaction among different mechanisms. Compressive stress in the film recommended in this work is based on the indentation-induced

interfacial delamination mechanism, that are exposed in the literature [69,70]. The deformation behavior of the NiTi/Ag bilayer should be first understood to evaluate the crack beginning and extension along the interface. For this purpose, the deformation stages of the NiTi/Ag system in an nanoindentation process are shown in Fig. 16. As can be seen from Fig. 16, the three illustrative deformation arrangements detected from the loading of nanoindentation [19], (i) the film and the substrate were firstly distorted elastically under compression. As the load was higher than a threshold value, the slip bands were made in the substrate (NiTi) and owing to the plane slip, “pop-in” event is relevant to the load–depth curve. (ii) Due to the mismatch in elasticity and the variance in plastic deformation between the film and substrate, phase tension was built up at the interface. Both film and the substrate were recovered elastically during unloading. (iii) When the tensile stress at the interface is overstepped, the interfacial delamination is happened, and a crack is appeared at the interface and distributed rapidly along it. As a consequence, the film was then separated from the substrate, leading to the observation of a “pop-out” [19].

#### 3.5.1. The Griffith energy balance concept

The concept of Griffith energy balance concept is engaged to examine the energy equilibrium at interfacial delamination to attain the energy released from delamination ( $U_s$ ) and the energy release rate  $G_{\text{in}}$  of the NiTi/Ag interface [71,72]. It was supposed that the interfacial fracture happened in the NiTi/Ag structures plays as a reversible thermodynamic factor, where the film and substrate were reflected as two elastic bodies. As mentioned in other experimental studies, for some film/substrate systems showing the strong interfacial adhesion, the interfacial delamination could not induce by standard nanoindentation. Hence, cyclic loading indentation had to be used. This technique has been applied in literature to delaminate the film/substrate structures. For example, the interfacial delamination behavior of TiN, AlN and SiC films are examined by cyclic indentation [73,74]. Therefore, this method can be applied to substitute the former monotonic loading nanoindentation, as the magnitudes of  $G_{\text{in}}$  are in good agreement with those obtained from previous method [28]. For such a system, the net energy of a static crack can be expressed as:

$$U = -U_e + U_s + W_d \quad (9)$$

where  $U_e$  is the strain energy stored in the elastic medium,  $U_s$  is the free energy needed to produce the whole crack surface, and  $W_d$  is the

**Table 3**

The results of  $E_{\text{plastic}}$  obtained for all bilayers with the different crystallographic orientations of the NiTi.

NiTi/Ag bilayers	$E_{\text{plastic}} (\mu\text{J})$
NiTi(2 1 1)/Ag	$103.63 \times 10^{-3}$
NiTi(3 2 1)/Ag	$269.46 \times 10^{-3}$
NiTi(1 0 0)/Ag	$285.02 \times 10^{-3}$
NiTi(2 1 0)/Ag	$297.64 \times 10^{-3}$
NiTi(1 1 1)/Ag	$300.07 \times 10^{-3}$
NiTi(0 1 0)/Ag	$525.46 \times 10^{-3}$

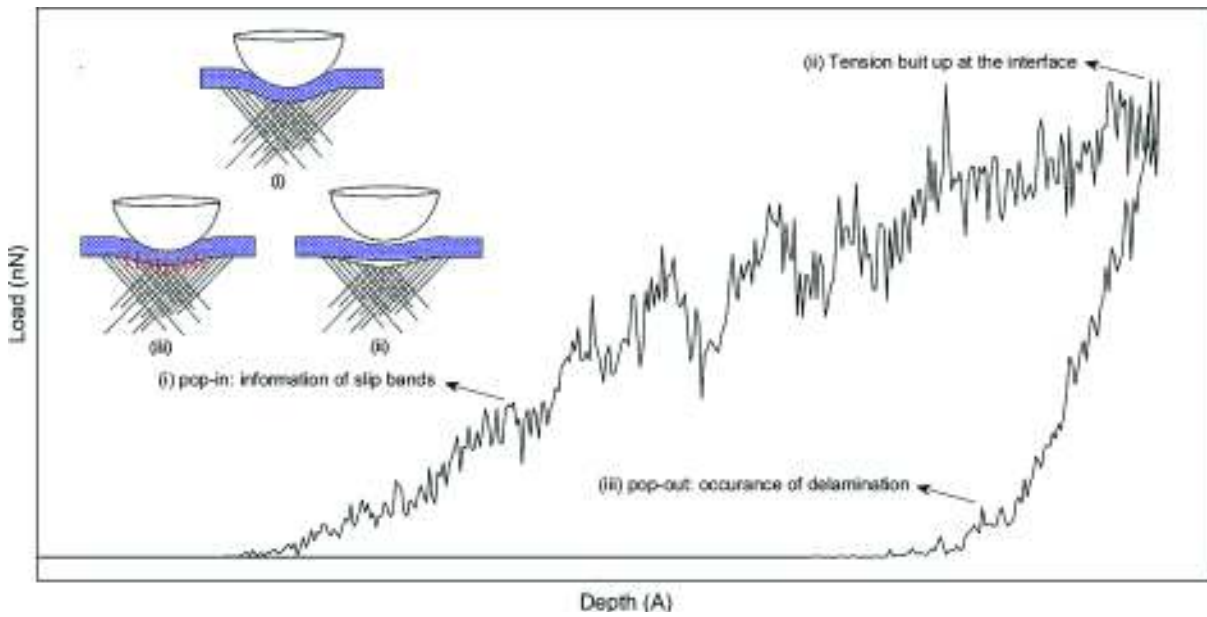


Fig. 16. The deformation stages of the NiTi/Ag bilayer in the nanoindentation process.

external mechanical work done via the indenter.

To obtain the thermodynamic equilibrium by balancing the three energy terms, it is essential that:

$$U = 0 \tag{10}$$

Thus, the energy required at the interfacial surface of crack can be achieved by rearranging Eq. (9) as:

$$U_s = U_e - W_d \tag{11}$$

The load-depth curve of the dual-indentation can be used to obtain the energy required for delamination, as presented in Fig. 17. The primary portion of the second loading indentation curve is contained by the responses of the detached film to elastic bending followed by the elastic deformation of both Ag and NiTi (curve OC'). Consequently, the stored energy of elastic strain the deflected film at  $h = h_c$  can be obtained by the area beneath the curve OC', i.e., the area encircled by OC'CC''O. As well as, integration of the unloading segment above the corresponding displacement range of  $h_0-h_c$  (the area surrounded by OCC''O), can be used for calculating the equivalent mechanical work

$W_d$  induced by the indenter. The initial stage of the unloading is nearly elastic. This behavior is in agreement with that seen generally in indentation experiments [75]. Careful examination has revealed that the existence of the pop-out incident at the end, near to the second unloading curve, should be relevant to the additional extension of the interfacial crack, showed by Lu et al. in similar event [28]. However, in this study, the crack generated in the secondary nanoindentation due to the complex nature of the crack propagation has been ignored, and we focused only on the crack produced in the first nanoindentation. Hence, according to Eq. (11), the surface energy  $U_s$  can be achieved through computing the area enclosed by OC'CO curves.

The calculation of the delamination area is discussed here. The incremental growth of the surface energy of the crack ( $dU_s$ ) and its extension ( $dA$ , in a film/substrate system having an interfacial crack of area  $A$ ) can be expressed as the energy release rate, i.e. [76,77],

$$G_{in} = \frac{dU_s}{dA} = \frac{U_s}{A} \tag{12}$$

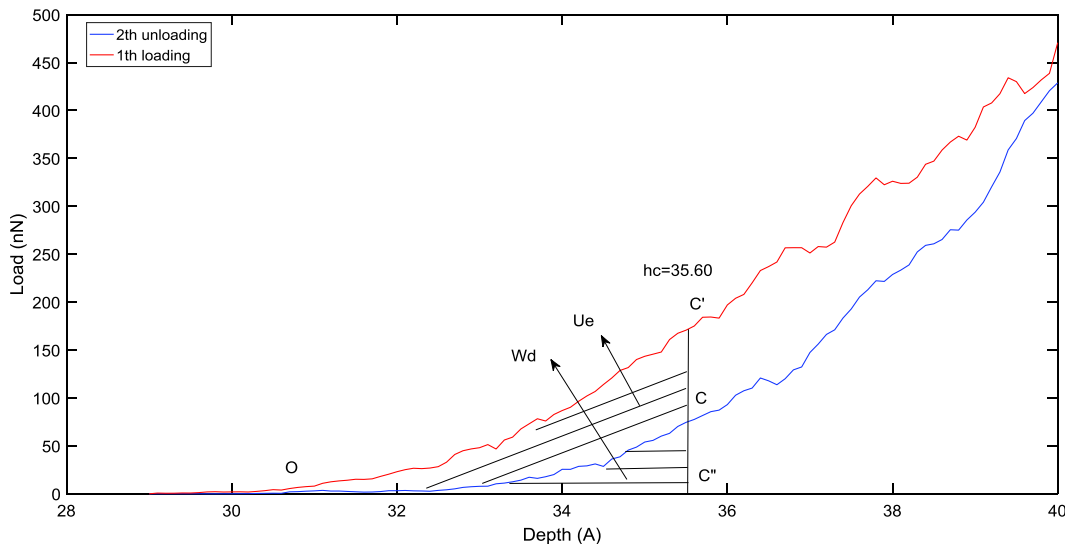


Fig. 17. Illustration of the energy calculation for indention-induced delamination.

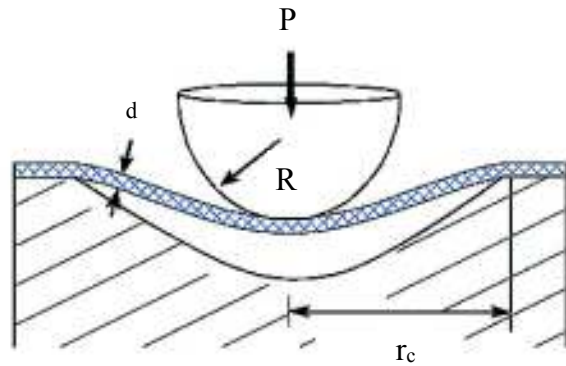


Fig. 18. The centrally loaded clamped circular plate model for delamination area estimation.

### 3.5.2. Determination of the delamination area

The measurement of the delamination area ( $A$ ) is difficult when the interfacial delamination happens under the film layers. Therefore, in order to calculate the energy release rate according to Eq. (12), the delaminated area ( $A$ ) should be determined. It is difficult to measure straightly the geometry of an interfacial crack under the film or substrate. Nevertheless, if an axisymmetric indenter is employed, the interfacial crack made due to indentation-induced delamination could estimate a diaphragm clamped on a circular boundary by evaluating the deflection of the diaphragm underneath an nanoindentation load, allowing us to compute the radius [see Fig. 18]. The correlation between an nanoindentation load and the consequential deflection of the clamped diaphragm below the load of  $P$  is followed by [23]:

$$h = \left( \frac{9P^2}{16RE^2} \right)^{1/3} + \frac{3Pr_c^2(1 - \nu^2)}{4\pi Ed^3} \quad (13)$$

where  $h$  is the indentation depth,  $P$  is the load,  $R$  is the indenter tip radius,  $E$  is the elastic modulus of the film,  $r_c$  is the crack radius,  $d$  and  $\nu$  are the thickness and the Poisson's ratio of the film.

$G_{in}$  can be considered as below, when  $r_i$  is identified:

$$G_{in} = \frac{U_s}{A} = \frac{U_e - W_d}{\pi r_i^2} \quad (14)$$

The interfacial toughness ( $K_{in}$ ) is associated with the equation of  $K_{in} = \sqrt{G_{in}E_{in}}$ , where  $E_{in}$  is representative Young's modulus for the coating/substrate system [21].

As can be understood from the results of both experiment and simulation works [69,70] the presence of a quite strong interface (but still much weaker than the coating and substrate) can cause the failure of the coating during unloading rather than loading [78]. On the other hand, the nanoindentation load was inadequately great to encourage delamination; our simulation results show that the fracture or cracking is not exposed in six NiTi/Ag bilayers through nanoindentation, whereas the maximum load of indentation exceeds half of the whole thickness of the NiTi/Ag bilayer. It was also postulated that the interface was too tough to be separated from the substrate by the present load of 567.334 nN. Nevertheless, the discontinuity in the corresponding unloading-depth curve in all cases (Fig. 15) implies that a little interfacial fracture between film and substrate is occurred, which is agreement with the experimental results reported by An et al. [79] In order to more discuss the occurrence of interfacial fracture in all bilayers, the values of  $W_d$ ,  $U_e$ ,  $G_{in}$ , and  $K_{in}$  are calculated for all systems, and the results are listed in Table 4. As shown, for all bilayers, the values of  $U_e$ ,  $W_d$ ,  $G_{in}$ , and  $K_{in}$  are changed from 233.371 to 731.423 nJ, 96.614 to 225.98 nJ, 23.375 to 147.711 J/nm<sup>2</sup> and 43.66 to 109.76 N/m<sup>2</sup>, respectively. It is important to emphasize here that in the films with the same thickness, the values of  $G_{in}$  and  $K_{in}$  are appeared to be

Table 4

The amounts of energy release during delamination ( $U_e$ ), external mechanical work ( $W_d$ ), energy release rate ( $G_{in}$ ) and interfacial toughness of the NiTi/Ag bilayers at the different crystallographic orientations of the substrate.

NiTi/Ag bilayers	$U_e$ (nJ)	$W_d$ (nJ)	$G_{in}$ (J/m <sup>2</sup> )	$K_{in}$ (N/m <sup>2</sup> )
NiTi(2 1 1)/Ag	731.423	220.07	147.711	109.76294
NiTi(3 2 1)/Ag	544.012	208.93	82.111	81.839709
NiTi(1 0 0)/Ag	492.914	225.984	64.279	72.409554
NiTi(2 1 0)/Ag	450.742	122.234	54.936	66.938785
NiTi(1 1 1)/Ag	395.244	155.542	38.892	56.324365
NiTi(0 1 0)/Ag	233.371	96.614	23.375	43.6640888

dependent on the crystallographic orientation of the substrate. However, the value of  $G_{in}$  and consequently the interfacial toughness of bilayers decreases in the following trend: NiTi (2 1 1) > NiTi (3 2 1) > NiTi (1 0 0) > NiTi (2 1 0) > NiTi (1 1 1) > NiTi (0 1 0).

Variation of the interfacial toughness of the bilayers was caused by a misfit strain due to misfit dislocation or other interface faults, as observed by Izadi [80] for Al/Ti layers. It is notable that the generation of elastic misfit strain and formation of misfit dislocations on the interface are due to the mismatch parameter of the adjacent layers of materials. The presence of elastic misfit strain and misfit dislocation along the interface can expand the unsteadiness of interface. Thus, it affects considerably the delamination mechanisms of NiTi/Ag bilayer. It is noteworthy that the dislocation nucleation and release of dislocations in the upper and lower films, as well as, the interaction of nucleated dislocations with the misfit dislocations and interface have a connection with the crystallographic orientation and the film thickness of NiTi/Ag bilayers. It is postulated that the connection of silver and the atoms of NiTi alloy as aligned at the different faces, can generate some misfit dislocations at the NiTi-Ag interface. This behavior is attributed to the fact that the increase in the interaction of dislocations at the interface is caused an increase in the interfacial toughness. As a result, the number of practical barriers for crack propagation [81] should lead to higher values of  $G_{in}$  and  $K_{in}$ . According to the states' arguments, it is clear that the NiTi (2 1 1)/Ag bilayer with higher energy released during nanoindentation process has the greatest misfit dislocation at the interface. Thus, it can be concluded that the NiTi (2 1 1)/Ag bilayer due to more interfacial toughness, is more favorable for engineering and medical applications. Also, the results reveal that the difference in the value of  $G_{in}$  in the film/substrate with different crystallographic orientation could be attributed to the mismatch in elastic-plastic properties of the film and substrate induced by the tension built up at the interface. In other words, the deformation patterns were also influenced by the crystallographic orientation in film/substrate bilayer with stronger mismatch between the film and substrate, requiring higher load for delamination of fracture [26,75,82]. As a result, it is postulated that the NiTi (2 1 1)/Ag with higher load for delamination (559.26 nN) has stronger mismatch between the film and the substrate.

To better understanding the delamination mechanism during the cyclic nanoindentation, it is essential to explore the relationship between the energy delamination and the hardness of the bilayers. The mechanical properties of the substrate play the main role to control the interfacial toughness. The relationship between the hardness and interfacial toughness of each bilayer is presented in Fig. 19a. The results show that the interfacial toughness is increased with the hardness. Among the six types of NiTi/Ag bilayers, the NiTi (2 1 1)/Ag and NiTi (0 1 0)/Ag are shown the biggest and lowest hardness, respectively (Table 1). Therefore, it was postulated that the NiTi (2 1 1)/Ag could have less plastic deformation, while the NiTi (0 1 0) substrate is plastically deformed. This behavior means that more elasticity can happen during unloading in the NiTi (2 1 1) than that of NiTi (0 1 0) substrate, which could subsequently result in adequate residual elastic strain energy to start interfacial delamination in the case of NiTi (2 1 1)/Ag. A similar observation was established by Mingyuan et al. [19] for the

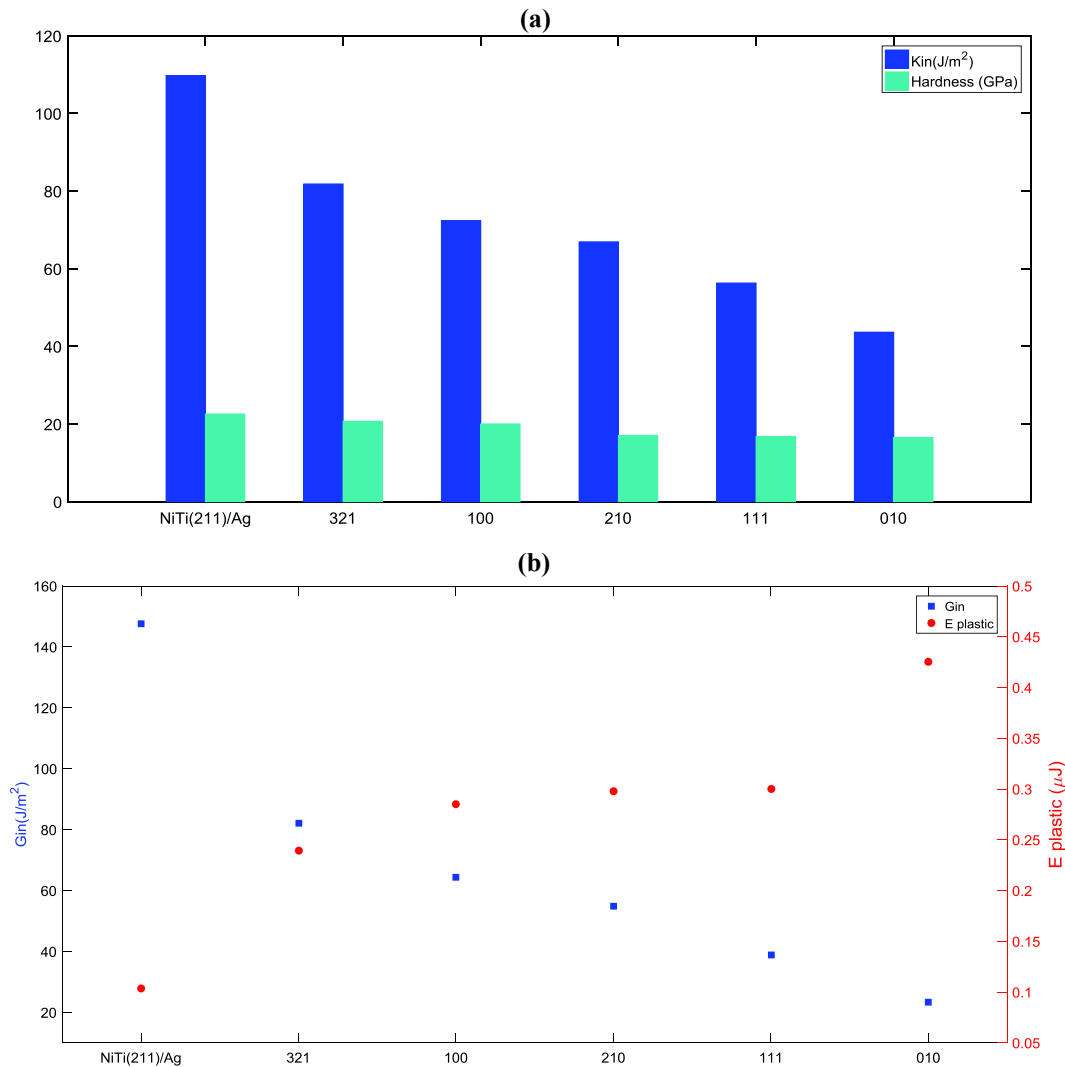


**Fig. 19.** (a) The relationship between the energy release rate ( $G_{in}$ ) and the plastic dissipation energy ( $E_{plastic}$ ) computed for NiTi/Ag bilayers. (b) The association between the hardness and interfacial toughness of the NiTi/Ag bilayers.

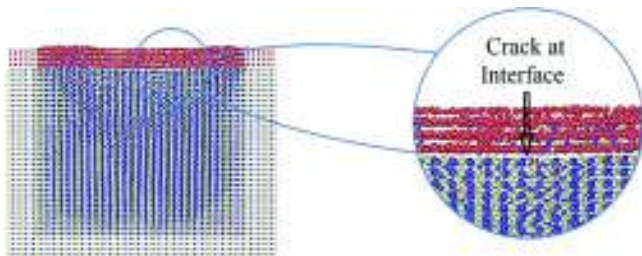


**Fig. 20.** An atomistic schematic of the indentation-induced interfacial delamination of the NiTi (0 1 0)/Ag bilayer.

GaAs/SiN multilayer. Generally, harder bilayer should have lower plastic dissipation energy (section 3.4), and larger value of  $G_{in}$ . Fig. 19b shows the association between the energy release rate ( $G_{in}$ ) and the plastic dissipation energy ( $E_{plastic}$ ) computed for all bilayers. This figure indicates that, if the value of  $E_{plastic}$  comes up, the energy release rate during unloading indentation would decrease. In summary, the resistance to interfacial cracking of the NiTi (2 1 1)/Ag bilayer due to the higher interfacial toughness is superior to that of the other bilayers. A reverse behavior for interfacial delamination is observed when the cyclic-nanoindentation for the NiTi (0 1 0)/Ag is conducted. Among the six types of NiTi/Ag bilayers studied here, the NiTi (0 1 0)/Ag has the

lowest hardness and interfacial toughness. Therefore, it is expected that this bilayer could experience the highest rate of cracking at the interface. An atomistic schematic of interfacial delamination behavior for NiTi (0 1 0)/Ag is presented in Fig. 20.

### 3.6. Changes of free energy during the test of nanoindentation in NiTi/Ag

The most critical concept to investigate the effect of crystallographic orientation is calculation of free energy which could be derived from Jarzynski's equality (JE) using MD simulation. It is important to know how free energy changes as a function of either an external parameter or internal coordinate [34]. Although the results of nanoindentation could support a series of metals and surface orientations, their impact on the change of free energy during nanoindentation has been never investigated.

The key of the Jarzynski's method is to select a nonequilibrium process such as nanoindentation and at the same time-limit the work fluctuation in each group of the nonequilibrium trajectories within the order of  $k_bT$  [83]. However, Jarzynski's equality could give the good results which has been verified for numerous thermodynamic ensembles and diverse groups of experimentally tested assumption [33]. Consequently, the range of thermodynamic free energy change is extracted from Jarzynski's equality:

**Table 5**

The free energy change obtained during non-equilibrium nanoindentation process of the NiTi/Ag at different crystallographic orientations of the NiTi.

NiTi/Ag bilayers	Free energy Change (eV/atom)	Free energy Change (J/atom)
NiTi(211)/Ag	$7.93 \times 10^{-4}$	$1.26 \times 10^{-22}$
NiTi(321)/Ag	$7.53 \times 10^{-4}$	$1.20 \times 10^{-22}$
NiTi(100)/Ag	$7.01 \times 10^{-4}$	$1.12 \times 10^{-22}$
NiTi(210)/Ag	$6.12 \times 10^{-4}$	$9.79 \times 10^{-23}$
NiTi(111)/Ag	$5.37 \times 10^{-4}$	$8.59 \times 10^{-23}$
NiTi(010)/Ag	$4.06 \times 10^{-4}$	$6.49 \times 10^{-23}$

$$\langle e^{-\beta W_\gamma} \rangle_N \equiv \int dW_\gamma \rho(W_\gamma) e^{-\beta W_\gamma} = e^{-\beta \Delta F} \quad (15)$$

where  $\beta = (1/k_b T)$ ,  $k_b$  is the Boltzmann constant and  $T$  is the temperature of the system in the equilibrium state.  $\Delta F$  is the change of the free energy of the system. The symbol  $\langle \dots \rangle_N$  represents an average over the realization of the process, and the equality is exact as  $N \rightarrow \infty$ . The nonequilibrium work distribution  $\rho(W_\gamma)$  depends on the schedule for varying the work parameter,  $\gamma$ , which is the external perturbation. The mentioned equality is simple; the equation involves the thermodynamic work done on the system by the external force. It is a work parameter controlled by  $W_\gamma = \int F dy$ .

We compare the values of the free energy of NiTi/Ag with different NiTi orientations to find any effect of the surface orientation of NiTi on these values. During the investigation of the free energies of the coatings with different orientations of the NiTi at the same number of silver deposited layers, this state can be explained by the presence of an interface which could reflect the strong interactions between Ag and atoms of NiTi at (211) face. Table 5 indicates the values of free energy of the NiTi/Ag with different orientations of the NiTi.

The data of Table 5 shows interestingly that the value of  $\Delta F$  for NiTi (211)/Ag sample is larger than that of other samples studied in this work. In other words, the NiTi/Ag bilayer with NiTi substrate at (211) face requires much more free energy to carry out the nanoindentation process. Therefore, higher thermodynamic work is needed to attain the same indentation depth in comparison with the other bilayers systems. In this system, the measured values of  $\Delta F$  are decreased in the following trend: NiTi (211) > NiTi (321) > NiTi (100) > NiTi (210) > NiTi (111) > NiTi (010). As the main result, the NiTi (211)/Ag bilayer due to more interfacial toughness, hardness and less plastic energy dissipation shows more change in the value of free energy during nanoindentation.

#### 4. Conclusions

This simulation advanced our understanding of the nature of NiTi/Ag bilayer according to the atomic-based mechanism of the plastic deformation and interfacial delamination. Our study is devoted by cyclic nanoindentation-induced delamination along the interface between the NiTi substrate as aligned at (100), (111), (110), (321), (210) and (211) faces and Ag film. We considered the determination of atomistic mechanism of the plastic deformation of NiTi/Ag bilayers and free energy calculations during the nanoindentation process via Jarzynski's equality using MD simulation. In this work, the interfacial toughness and the plastic energy dissipated in each loading-unloading cycle of NiTi/Ag bilayers were obtained from cyclic loading nanoindentation simulation. The energy released from interfacial delamination and the delamination areas were obtained by an analytical model that is based on the Griffith energy conservation theory and clamped circular plate model. The conclusions can be summarized as follows:

1- Two distinct mechanisms are recognized to be responsible for the plastic deformation of NiTi/Ag bilayers. Prismatic dislocation loop

and nest-like organization of twins were found responsible for the irreversible plastic conveyance of NiTi/Ag bilayers as NiTi aligned at (211,010,111) and (100,210,321) faces, respectively.

- The average dislocation densities encouraged by the radius of 30 Å of indenter at the indentation depth of  $h = 33 \text{ \AA}$ , were found in the range of  $1.23 \times 10^{19}$ – $1.84 \times 10^{19} \text{ m}^{-2}$ . The results reveal that the dislocation density induced by the nanoindentation of NiTi (010)/Ag was somewhat higher than that of other bilayers considered in this work. As a result, the key factor governing the densification at depth of 33 Å is the dislocation induced by loop formation mechanisms and dislocation densities calculated for NiTi/Ag as NiTi aligned at (010), (111) and (211) faces are higher than those of (100), (321) and (210) faces, respectively.
- The values of  $G_{in}$  and  $K_{in}$  of bilayers appear to be dependent on the crystallographic orientation of the substrate. These values are in the range of 23.37–147.71 J/m<sup>2</sup> and 43.66 – 109.76 N/m<sup>2</sup> for NiTi/Ag with the different crystallographic orientation of the substrate, respectively. The values of  $G_{in}$  and  $K_{in}$  values decrease also in the following trend: NiTi (211) > NiTi (321) > NiTi (100) > NiTi (210) > NiTi (111) > NiTi (010).
- Among the six samples tested here, the NiTi (211)/Ag and NiTi (010)/Ag cases have the most significant and lowest hardness, respectively. Therefore, it was concluded that the NiTi (211)/Ag has less plastic deformation, while the NiTi (010) substrate is deformed more.
- By the Jarzynski's equality on yielding in bilayers, this search reveals that the changes of free energy are more appropriate for predicting the thermodynamic work needed for nanoindentation of NiTi/Ag bilayer. The NiTi/Ag bilayer with NiTi substrate aligned by (211) orientation requires also much more free energy to carry out the nanoindentation process. Therefore, more thermodynamic work is needed here to attain the same indentation depth in comparison with the other bilayers systems.
- The average plastic energy dissipated per cycle during cyclic nanoindentation in a NiTi/Ag bilayer with different crystallographic orientation is estimated. It is concluded that the increase of interfacial toughness of NiTi (211)/Ag could be the good factor to discuss the less plastic energy dissipation. The measured values of  $E_{plastic}$  increases in the following trend: NiTi (211) < NiTi (321) < NiTi (100) < NiTi (210) < NiTi (111) < NiTi (010). As well as, the values of plastic dissipation energy estimated for NiTi/Ag with different crystallographic orientations were consistent with the dislocation densities computed for all-bilayers at maximum indentation depth ( $h = 40 \text{ \AA}$ ).

Based on these results, it can be concluded that the selection of crystallographic orientation in the MD simulation should be made on a careful evaluation. As a significant result, the NiTi (211)/Ag bilayer due to more interfacial toughness, hardness, and less plastic energy dissipation is favorable for engineering and medical applications.

#### 5. Prime novelty statement

In the submitted manuscript, we are reporting, for the first time, the computational results obtained for cyclic nanoindentation test to be used for NiTi/Ag substrate/film with great potential for engineering and medical applications. The main objective of the article was to examine the effect of crystallographic orientation of NiTi on the plastic deformation mechanisms, the mechanical properties, the density dislocation and the plastic energy dissipation of the NiTi/Ag bilayers. Further, we have used the Griffith energy balance model to found the energy released for interfacial delamination of NiTi/Ag substrate/film with different crystallographic orientation of substrate. We are also reporting the free energy changes calculated by Jarzynski's equality during nanoindentation of NiTi/Ag bilayer when NiTi aligned (100), (111), (110), (321), (210) and (211) faces. These calculations are

useful for get a deeper insight into the cyclic nanoindentation results. These results suggest that the NiTi (2 1 1)/Ag bilayer due to having more interfacial toughness, hardness, and less plastic energy dissipation is favorable for engineering and medical applications. In view to this, the publication of this work in Journal of Computational Materials Science will be valuable.

## Acknowledgments

The authors would like to express their sincere appreciation to the Iran National Science Foundation (INSF) for support of the research under Grant 96006124.

### Data availability

The data required to reproduce these findings are from part of an ongoing study. However, they can be made available on request.

## Appendix A. Supplementary data

Supplementary data to this article can be found online at <https://doi.org/10.1016/j.commat.2019.05.032>.

## References

- [1] S. Hao, L. Cui, J. Jiang, F. Guo, X. Xiao, D. Jiang, C. Yu, Z. Chen, H. Zhou, Y. Wang, Y. Liu, D.E. Brown, Y. Ren, A novel multifunctional NiTi/Ag hierarchical composite, *Sci. Rep.* 4 (2014) 5267, <https://doi.org/10.1038/srep05267>.
- [2] S. Weng, H. Ning, N. Hu, C. Yan, T. Fu, X. Peng, S. Fu, J. Zhang, C. Xu, D. Sun, Y. Liu, L. Wu, Strengthening effects of twin interface in Cu/Ni multilayer thin films – a molecular dynamics study, *Mater. Des.* 111 (2016) 1–8, <https://doi.org/10.1016/j.matdes.2016.08.069>.
- [3] P. Li, X. Zhang, R. Xu, W. Wang, X. Liu, K.W.K. Yeung, P.K. Chu, Electrochemically deposited chitosan/Ag complex coatings on biomedical NiTi alloy for antibacterial application, *Surf. Coatings Technol.* 232 (2013) 370–375, <https://doi.org/10.1016/j.surfcoat.2013.05.037>.
- [4] M. Saugó, D.O. Flamini, L.I. Brugnoni, S.B. Saidman, Silver deposition on polypyrrole films electrosynthesised onto Nitinol alloy. Corrosion protection and antibacterial activity, *Mater. Sci. Eng. C.* (2015), <https://doi.org/10.1016/j.msec.2015.06.014>.
- [5] D. Zhao, H. Zhao, B. Zhu, S. Wang, Investigation on hardening behavior of metallic glass under cyclic indentation loading via molecular dynamics simulation, *Appl. Surf. Sci.* (2017), <https://doi.org/10.1016/j.apsusc.2017.04.125>.
- [6] A. Kumar, D. Singh, R. Kumar, D. Kaur, Effect of crystallographic orientation of nanocrystalline TiN on structural, electrical and mechanical properties of TiN/NiTi thin films, *J. Alloys Compd.* 479 (2009) 166–172, <https://doi.org/10.1016/j.jallcom.2008.12.116>.
- [7] N.H. Faisal, A.K. Prathuru, S. Goel, R. Ahmed, M.G. Droubi, B.D. Beake, Y.Q. Fu, Cyclic Nanoindentation and nano-impact fatigue mechanisms of functionally graded TiN/TiNi film, *Shape Mem. Superelasticity* 3 (2017) 149–167, <https://doi.org/10.1007/s40830-017-0099-y>.
- [8] L.L. Meisner, A.I. Lotkov, V.A. Matveeva, L.V. Artemieva, S.N. Meisner, A.L. Matveev, Effect of silicon, titanium, and zirconium ion implantation on NiTi biocompatibility, *Adv. Mater. Sci. Eng.* (2012), <https://doi.org/10.1155/2012/706094>.
- [9] P. Luo, S.N. Wang, T.T. Zhao, Y. Li, Surface characteristics, corrosion behavior, and antibacterial property of Ag-implanted NiTi alloy, *Rare Met.* (2013), <https://doi.org/10.1007/s12598-013-0041-1>.
- [10] L. Zhao, H. Wang, K. Huo, L. Cui, W. Zhang, H. Ni, Y. Zhang, Z. Wu, P.K. Chu, Antibacterial nano-structured titania coating incorporated with silver nanoparticles, *Biomaterials* (2011), <https://doi.org/10.1016/j.biomaterials.2011.04.040>.
- [11] J. Li, H. Zheng, T. Sinkovits, A.C. Hee, Y. Zhao, Mono- and multiple TiN(Ti) coating adhesion mechanism on a Ti–13Nb–13Zr alloy, *Appl. Surf. Sci.* 355 (2015) 502–508, <https://doi.org/10.1016/j.apsusc.2015.07.126>.
- [12] X. Zha, F. Jiang, X. Xu, Investigation of modelling and stress distribution of a coating/substrate system after an indentation test, *Int. J. Mech. Sci.* 134 (2017) 1–14, <https://doi.org/10.1016/j.ijmecsci.2017.10.002>.
- [13] L. Xie, P. Brault, A.L. Thomann, L. Bedra, Molecular dynamic simulation of binary ZrxCu100-xmetallic glass thin film growth, *Appl. Surf. Sci.* (2013), <https://doi.org/10.1016/j.apsusc.2013.03.004>.
- [14] B. Reischl, A.L. Rohl, A. Kurosen, K. Nordlund, Atomistic simulation of the measurement of mechanical properties of gold nanorods by AFM, *Sci. Rep.* (2017), <https://doi.org/10.1038/s41598-017-16460-9>.
- [15] M. Lu, H. Huang, Interfacial energy release rates of SiN/GaAs film/substrate systems determined using a cyclic loading dual-indentation method, *Thin Solid Films* (2015), <https://doi.org/10.1016/j.tsf.2015.07.027>.
- [16] A. Abdul-Baqi, E. Van Der Giessen, Indentation-induced interface delamination of a strong film on a ductile substrate, *Thin Solid Films* (2001), [https://doi.org/10.1016/S0040-6090\(00\)01344-4](https://doi.org/10.1016/S0040-6090(00)01344-4).
- [17] R. Pejman, S.H. Salehi, M. Salehi, Numerical study of interfacial crack growth effects on nanoindentation mechanical properties in presence of pre-existing defect, *Thin Solid Films* (2013), <https://doi.org/10.1016/j.tsf.2013.08.033>.
- [18] S.M. Xia, Y.F. Gao, A.F. Bower, L.C. Lev, Y.T. Cheng, Delamination mechanism maps for a strong elastic coating on an elastic-plastic substrate subjected to contact loading, *Int. J. Solids Struct.* (2007), <https://doi.org/10.1016/j.ijssolstr.2006.10.009>.
- [19] M. Lu, H. Xie, H. Huang, J. Zou, Y. He, Indentation-induced delamination of plasma-enhanced chemical vapor deposition silicon nitride film on gallium arsenide substrate, *J. Mater. Res.* (2013), <https://doi.org/10.1557/jmr.2013.31>.
- [20] P. Lu, X. Xiao, Y.K. Chou, Interface delamination study of diamond-coated carbide tools considering coating fractures, *Surf. Coat. Technol.* (2014), <https://doi.org/10.1016/j.surfcoat.2014.08.080>.
- [21] J. Chen, S.J. Bull, Approaches to investigate delamination and interfacial toughness in coated systems: an overview, *J. Phys. D: Appl. Phys.* (2011), <https://doi.org/10.1088/0022-3727/44/3/034001>.
- [22] S.V. Hainsworth, M.R. McGurk, T.F. Page, The effect of coating cracking on the indentation response of thin hard-coated systems, *Surf. Coat. Technol.* (1998), [https://doi.org/10.1016/S0257-8972\(97\)00683-X](https://doi.org/10.1016/S0257-8972(97)00683-X).
- [23] H. Xie, H. Huang, Characterization of the interfacial strength of SiN<sub>x</sub>/GaAs film/substrate systems using energy balance in nanoindentation, *J. Mater. Res.* (2013), <https://doi.org/10.1557/jmr.2013.317>.
- [24] H. Huang, K.J. Winchester, A. Suvorova, B.R. Lawn, Y. Liu, X.Z. Hu, J.M. Dell, L. Faraone, Effect of deposition conditions on mechanical properties of low-temperature PECVD silicon nitride films, *Mater. Sci. Eng. A.* (2006), <https://doi.org/10.1016/j.msea.2006.07.015>.
- [25] Z. Wang, S. Tsukimoto, M. Saito, Y. Ikuhara, SiC/Ti<sub>3</sub>SiC<sub>2</sub> interface: Atomic structure, energetics, and bonding, *Phys. Rev. B* 79 (2009) 45318, <https://doi.org/10.1103/PhysRevB.79.045318>.
- [26] Q. Zhou, Y. Ren, Y. Du, D.P. Hua, W.C. Han, Q.S. Xia, Adhesion energy and related plastic deformation mechanism of Cu/Ru nanostructured multilayer film, *J. Alloys Compd.* 772 (2019) 823–827, <https://doi.org/10.1016/j.jallcom.2018.09.111>.
- [27] R. Sun, Z. Wang, M. Saito, N. Shibata, Y. Ikuhara, Atomistic mechanisms of non-stoichiometry-induced twin boundary structural transformation in titanium dioxide, *Nat. Commun.* (2015), <https://doi.org/10.1038/ncomms8120>.
- [28] M. Lu, H. Huang, Determination of the energy release rate in the interfacial delamination of silicon nitride film on gallium arsenide substrate via nanoindentation, *J. Mater. Res.* (2014), <https://doi.org/10.1557/jmr.2014.41>.
- [29] S.S. Chiang, D.B. Marshall, A.G. Evans, The response of solids to elastic/plastic indentation. I. Stresses and residual stresses, *J. Appl. Phys.* 53 (1982) 298–311.
- [30] M.V. Swain, J. Menčík, Mechanical property characterization of thin films using spherical tipped indenters, *Thin Solid Films.* (1994), [https://doi.org/10.1016/0040-6090\(94\)90321-2](https://doi.org/10.1016/0040-6090(94)90321-2).
- [31] K. Gall, H. Sehitoglu, Role of texture in tension-compression asymmetry in polycrystalline NiTi, *Int. J. Plast.* (1999), [https://doi.org/10.1016/S0749-6419\(98\)00060-6](https://doi.org/10.1016/S0749-6419(98)00060-6).
- [32] C.D. Christ, A.E. Mark, W.F. Van Gunsteren, Basic ingredients of free energy calculations: a review, *J. Comput. Chem.* (2010), <https://doi.org/10.1002/jcc.21450>.
- [33] I. Echeverria, L.M. Amzel, Estimation of free-energy differences from computed work distributions: an application of Jarzynski's equality, *J. Phys. Chem. B.* (2012), <https://doi.org/10.1021/jp300527q>.
- [34] S. Park, F. Khalili-Araghi, E. Tajkhorshid, K. Schulten, Free energy calculation from steered molecular dynamics simulations using Jarzynski's equality, *J. Chem. Phys.* (2003), <https://doi.org/10.1063/1.1590311>.
- [35] S. Fazeli, M. Vahedpour, S.K. Sadrnezhad, Comparison of the mechanical properties of NiTi/Cu bilayer by nanoindentation and tensile test: Molecular dynamics simulation, *Mater. Res. Express.* 3 (2016), <https://doi.org/10.1088/2053-1591/3/12/126504>.
- [36] S. Plimpton, Fast parallel algorithms for short-range molecular dynamics, *J. Comput. Phys.* (1995), <https://doi.org/10.1006/jcph.1995.1039>.
- [37] R.L. Davidchack, R. Handel, M.V. Tretyakov, Langevin thermostat for rigid body dynamics, *J. Chem. Phys.* (2009), <https://doi.org/10.1063/1.3149788>.
- [38] X. Huang, G.J. Ackland, K.M. Rabe, Crystal structures and shape-memory behaviour of NiTi, *Nat. Mater.* (2003), <https://doi.org/10.1038/nmat884>.
- [39] X.W. Zhou, R.A. Johnson, H.N.G. Wadley, Misfit-energy-increasing dislocations in vapor-deposited CoFe/NiFe multilayers, *Phys. Rev. B.* 69 (2004) 144113, <https://doi.org/10.1103/PhysRevB.69.144113>.
- [40] A. Stukowski, V.V. Bulatov, A. Arsenlis, Automated identification and indexing of dislocations in crystal interfaces, *Model. Simul. Mater. Sci. Eng.* (2012), <https://doi.org/10.1088/0965-0393/20/8/085007>.
- [41] A. Stukowski, Visualization and analysis of atomistic simulation data with OVITO—the Open Visualization Tool, *Model. Simul. Mater. Sci. Eng.* (2010), <https://doi.org/10.1088/0965-0393/18/1/015012>.
- [42] A.L. Stevens, L. Davison, W.E. Warren, Spall fracture in aluminum monocrystals: a dislocation-dynamics approach, *J. Appl. Phys.* 43 (1972) 4922–4927.
- [43] M.A. Bhatia, K.N. Solanki, A. Moitra, M.A. Tschopp, The effect of crystallographic orientation on void growth: a molecular dynamics study, *Suppl. Proc. Mater. Fabr. Prop. Charact. Model.* (2011), <https://doi.org/10.1002/9781118062142.ch69>.
- [44] S.-R. Jian, Y.-C. Tseng, I.-J. Teng, J.-Y. Juang, Dislocation Energetics and Pop-Ins in AlN Thin Films by Berkovich Nanoindentation. *Mater.* (Basel, Switzerland), 2013. doi: 10.3390/ma6094259.
- [45] T. Fu, X. Peng, S. Weng, Y. Zhao, F. Gao, L. Deng, Z. Wang, Molecular dynamics simulation of effects of twin interfaces on Cu/Ni multilayers, *Mater. Sci. Eng. A.* 658 (2016) 1–7, <https://doi.org/10.1016/j.msea.2016.01.055>.
- [46] T. Fu, X. Peng, C. Huang, D. Yin, Q. Li, Z. Wang, Molecular dynamics simulation of VN thin films under indentation, *Appl. Surf. Sci.* (2015), <https://doi.org/10.1016/j.apsusc.2015.09.024>.

- [47] E.T. Lilleodden, J.A. Zimmerman, S.M. Foiles, W.D. Nix, Atomistic simulations of elastic deformation and dislocation nucleation during nanoindentation, *J. Mech. Phys. Solids*. (2003), [https://doi.org/10.1016/S0022-5096\(02\)00119-9](https://doi.org/10.1016/S0022-5096(02)00119-9).
- [48] Y. Lee, J.Y. Park, S.Y. Kim, S. Jun, S. Im, Atomistic simulations of incipient plasticity under Al(1 1 1) nanoindentation, *Mech. Mater.* (2005), <https://doi.org/10.1016/j.mechmat.2005.01.004>.
- [49] T. Fu, X. Peng, X. Chen, S. Weng, N. Hu, Q. Li, Z. Wang, Molecular dynamics simulation of nanoindentation on Cu/Ni nanotwinned multilayer films using a spherical indenter, *Sci. Rep.* 6 (2016) 35665, <https://doi.org/10.1038/srep35665>.
- [50] X. Li, Y. Wei, L. Lu, K. Lu, H. Gao, Dislocation nucleation governed softening and maximum strength in nano-twinned metals, *Nature* (2010), <https://doi.org/10.1038/nature08929>.
- [51] Y. Zhao, X. Peng, T. Fu, R. Sun, C. Feng, Z. Wang, MD simulation of nanoindentation on (001) and (111) surfaces of Ag-Ni multilayers, *Phys. E Low-Dimen. Syst. Nanostruct.* (2015), <https://doi.org/10.1016/j.physe.2015.08.020>.
- [52] C.J. Ruestes, A. Stukowski, Y. Tang, D.R. Tramontina, P. Erhart, B.A. Remington, H.M. Urbassek, M.A. Meyers, E.M. Bringa, Atomistic simulation of tantalum nanoindentation: effects of indenter diameter, penetration velocity, and interatomic potentials on defect mechanisms and evolution, *Mater. Sci. Eng. A*. (2014), <https://doi.org/10.1016/j.msea.2014.07.001>.
- [53] Z. You, X. Li, L. Gui, Q. Lu, T. Zhu, H. Gao, L. Lu, Plastic anisotropy and associated deformation mechanisms in nanotwinned metals, *Acta Mater.* (2013), <https://doi.org/10.1016/j.actamat.2012.09.052>.
- [54] J.H.A. Hagelaar, E. Bitzek, C.F.J. Flipse, P. Gumbsch, Atomistic simulations of the formation and destruction of nanoindentation contacts in tungsten, *Phys. Rev. B* 73 (2006) 45425, <https://doi.org/10.1103/PhysRevB.73.045425>.
- [55] K.T. Oh, U.H. Joo, G.H. Park, C.J. Hwang, K.N. Kim, Effect of silver addition on the properties of nickel-titanium alloys for dental application, *J. Biomed. Mater. Res. - Part B Appl. Biomater.* (2006), <https://doi.org/10.1002/jbm.b.30369>.
- [56] W. Wang, L. Li, C. Yang, R.A. Soler-Crespo, Z. Meng, M. Li, X. Zhang, S. Keten, H.D. Espinosa, Plasticity resulted from phase transformation for monolayer molybdenum disulfide film during nanoindentation simulations, *Nanotechnology* (2017), <https://doi.org/10.1088/1361-6528/aa656a>.
- [57] R. Saha, W.D. Nix, Effects of the substrate on the determination of thin film mechanical properties by nanoindentation, *Acta Mater.* (2002), [https://doi.org/10.1016/S1359-6454\(01\)00328-7](https://doi.org/10.1016/S1359-6454(01)00328-7).
- [58] R. Saha, W.D. Nix, Solt films on hard substrates – Nanoindentation of tungsten films on sapphire substrates, *Mater. Sci. Eng. A*. (2001), [https://doi.org/10.1016/S0921-5093\(01\)01076-0](https://doi.org/10.1016/S0921-5093(01)01076-0).
- [59] F. Sansoz, K.D. Stevenson, Relationship between hardness and dislocation processes in a nanocrystalline metal at the atomic scale, *Phys. Rev. B – Condens. Matter Mater. Phys.* (2011), <https://doi.org/10.1103/PhysRevB.83.224101>.
- [60] G.I. Taylor, The mechanism of plastic deformation of crystals. Part I. Theoretical, *Proc. R. Soc. A Math. Phys. Eng. Sci.* (1934), <https://doi.org/10.1098/rspa.1934.0106>.
- [61] J. Hua, A. Hartmaier, Determining Burgers vectors and geometrically necessary dislocation densities from atomistic data, *Model. Simul. Mater. Sci. Eng.* (2010), <https://doi.org/10.1088/0965-0393/18/4/045007>.
- [62] J.L. Zhang, S. Zaeferrer, D. Raabe, A study on the geometry of dislocation patterns in the surrounding of nanoindenters in a TWIP steel using electron channeling contrast imaging and discrete dislocation dynamics simulations, *Mater. Sci. Eng. A*. (2015), <https://doi.org/10.1016/j.msea.2015.03.078>.
- [63] K. Durst, B. Backes, M. Göken, Indentation size effect in metallic materials: correcting for the size of the plastic zone, *Scr. Mater.* (2005), <https://doi.org/10.1016/j.scriptamat.2005.02.009>.
- [64] S. Goel, G. Cross, A. Stukowski, E.G.-C.M., undefined 2018, Designing nanoindentation simulation studies by appropriate indenter choices: Case study on single crystal tungsten, Elsevier. (n.d.). <https://www.sciencedirect.com/science/article/pii/S0927025618302854> (accessed 8.02.19).
- [65] C. Chen, H. Li, H. Xiang, X. Peng, Molecular dynamics simulation on B3-GaN thin films under nanoindentation, *Nanomater* (Basel, Switzerland) 8 (2018) 856, <https://doi.org/10.3390/nano8100856>.
- [66] Y.L. Chiu, A.H.W. Ngan, A TEM investigation on indentation plastic zones in Ni3Al (Cr, B) single crystals, *Acta Mater.* (2002), [https://doi.org/10.1016/S1359-6454\(02\)00100-3](https://doi.org/10.1016/S1359-6454(02)00100-3).
- [67] S. Graça, R. Colaço, P.A. Carvalho, R. Vilar, Determination of dislocation density from hardness measurements in metals, *Mater. Lett.* (2008), <https://doi.org/10.1016/j.matlet.2008.04.072>.
- [68] F. Yang, L. Peng, K. Okazaki, Cyclic indentation in aluminum, *J. Mater. Sci.* (2007), <https://doi.org/10.1007/s10853-006-0480-2>.
- [69] J.W. Hutchinson, Z. Suo, Mixed Mode Cracking in Layered Materials, *Adv. Appl. Mech.* (1991), [https://doi.org/10.1016/S0065-2156\(08\)70164-9](https://doi.org/10.1016/S0065-2156(08)70164-9).
- [70] S.S. Chiang, D.B. Marshall, A.G. Evans, A simple method for adhesion measurements, *Surfaces Interfaces Ceram. Ceram. Syst. Springer*, 1981, pp. 603–617.
- [71] J. Chen, S.J. Bull, Indentation fracture and toughness assessment for thin optical coatings on glass, *J. Phys. D. Appl. Phys.* (2007), <https://doi.org/10.1088/0022-3727/40/18/S01>.
- [72] B. Lawn, *Fracture of Brittle Solids – second edition*, Sci. Ser. (1993), <https://doi.org/10.1017/CBO9780511623127>.
- [73] T.D. Raju, K. Nakasa, M. Kato, Relation between delamination of thin films and backward deviation of load-displacement curves under repeating nanoindentation, *Acta Mater.* (2003), [https://doi.org/10.1016/S1359-6454\(02\)00429-9](https://doi.org/10.1016/S1359-6454(02)00429-9).
- [74] T.D. Raju, M. Kato, K. Nakasa, Backward deviation and depth recovery of load-displacement curves of amorphous SiC film under repeating nanoindentation, *Acta Mater.* (2003), [https://doi.org/10.1016/S1359-6454\(03\)00176-9](https://doi.org/10.1016/S1359-6454(03)00176-9).
- [75] M.F. Doerner, W.D. Nix, A method for interpreting the data from depth-sensing indentation instruments, *J. Mater. Res.* (1986), <https://doi.org/10.1557/JMR.1986.0601>.
- [76] A. Abdul-Baqi, E. Van der Giessen, Delamination of a strong film from a ductile substrate during indentation unloading, *J. Mater. Res.* (2001), <https://doi.org/10.1557/JMR.2001.0195>.
- [77] J. Chen, S.J. Bull, Assessment of the adhesion of ceramic coatings, *Adv. Sci. Technol.* 45 (2006) 1299–1308, <https://doi.org/10.4028/www.scientific.net/AST.45.1299>.
- [78] F. Abadias, S. Dub, R. Shmegeera, Nanoindentation hardness and structure of ion beam sputtered TiN, W and TiN/W multilayer hard coatings, *Surf. Coatings Technol.* 200 (2006) 6538–6543, <https://doi.org/10.1016/j.surfcoat.2005.11.053>.
- [79] T. An, M. Wen, C.Q. Hu, H.W. Tian, W.T. Zheng, Interfacial fracture for TiN/SiNx nano-multilayer coatings on Si(111) characterized by nanoindentation experiments, *Mater. Sci. Eng. A*. 494 (2008) 324–328, <https://doi.org/10.1016/j.msea.2008.04.020>.
- [80] S. Izadi, H. Mraied, W. Cai, Tribological and mechanical behavior of nanostructured Al/Ti multilayers, *Surf. Coat. Technol.* 275 (2015) 374–383, <https://doi.org/10.1016/j.surfcoat.2015.04.039>.
- [81] P. Wicinski, J. Smolik, H. Garbacz, J. Bonarski, A. Mazurkiewicz, K.J. Kurzydowski, Microstructure and properties of metal/ceramic and ceramic/ceramic multilayer coatings on titanium alloy Ti6Al4V, *Surf. Coat. Technol.* (2017), <https://doi.org/10.1016/j.surfcoat.2016.11.003>.
- [82] N.J.M. Carvalho, J.T.M. De Hosson, Deformation mechanisms in TiN/(Ti, Al)N multilayers under depth-sensing indentation, *Acta Mater.* 54 (2006) 1857–1862, <https://doi.org/10.1016/j.actamat.2005.12.010>.
- [83] B. Wan, C. Yang, Y. Wang, X. Zhou, Jarzynski matrix equality: Calculating the free-energy difference by nonequilibrium simulations with an arbitrary initial distribution, *Phys. Rev. E*. (2016), <https://doi.org/10.1103/PhysRevE.93.043312>.